List of figures

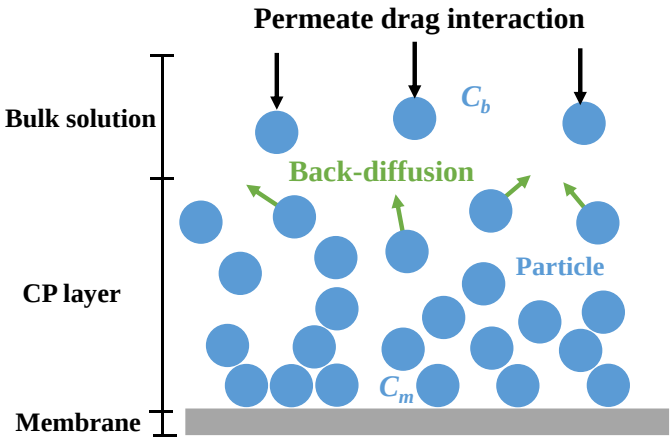

Fig. 1 CP and mass transfer during membrane filtration

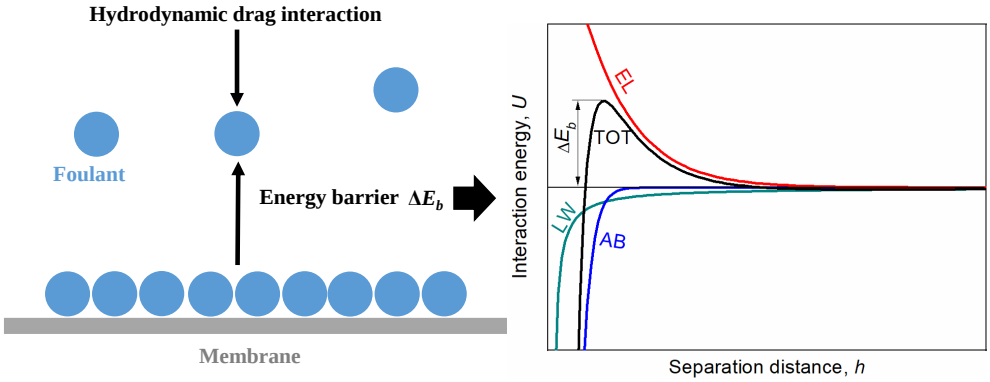

Fig. 2 Interactions acting on particles in colloidal attachment stage

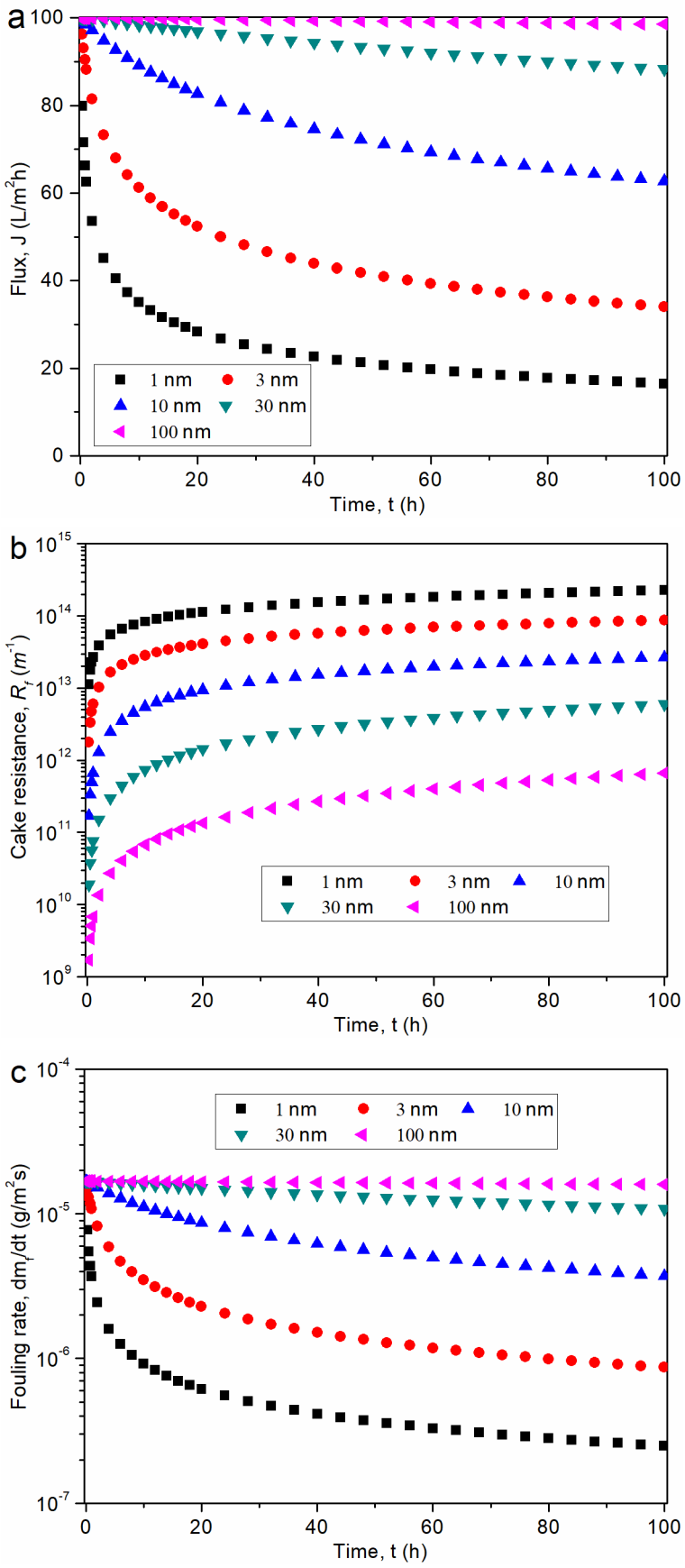

Fig. 3 Effect of colloidal particle size on fouling from the aspect of specific cake

resistance. The dependence of α_f on d_p is determined according to Eq. 22. The value of D, k_m, ΔE_d and ΔE_b are fixed at 4.91×10^{-11} m^2/s, 1.02×10^{-5} m/s, $4.19 \times 10^{-17} \times J$ and $5k_BT$, respectively. See other parameters in Table 1.

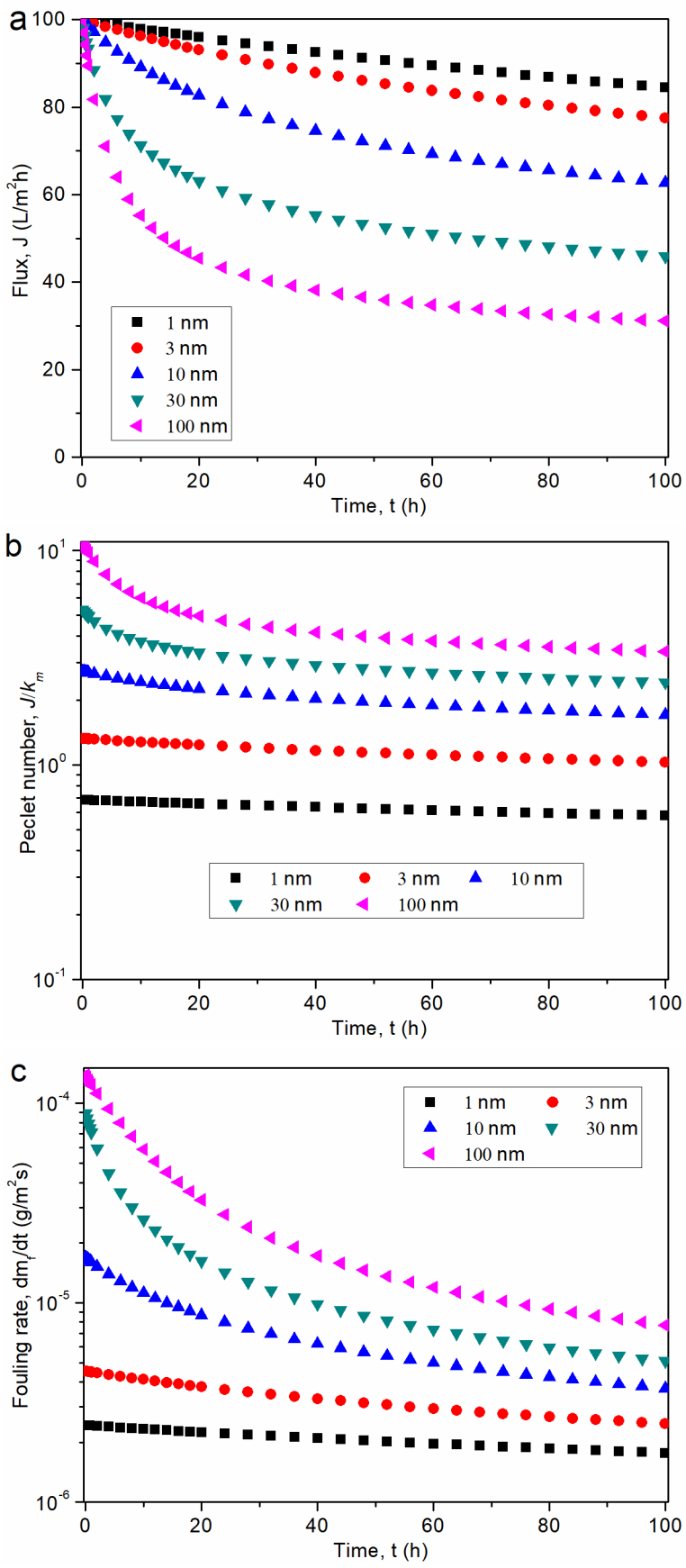

Fig. 4 Effect of colloidal particle size on fouling from the aspect of particle back-

diffusion and mass transfer coefficient. The dependence of D and k_m on d_p is determined according to Eq. 15 and Eq. 11, respectively. The value of α_f, ΔE_d and ΔE_b are fixed at 1.13×10^{13} m/g, $4.19 \times 10^{-17} \times J$ and $5k_BT$, respectively. See other parameters in Table 1.

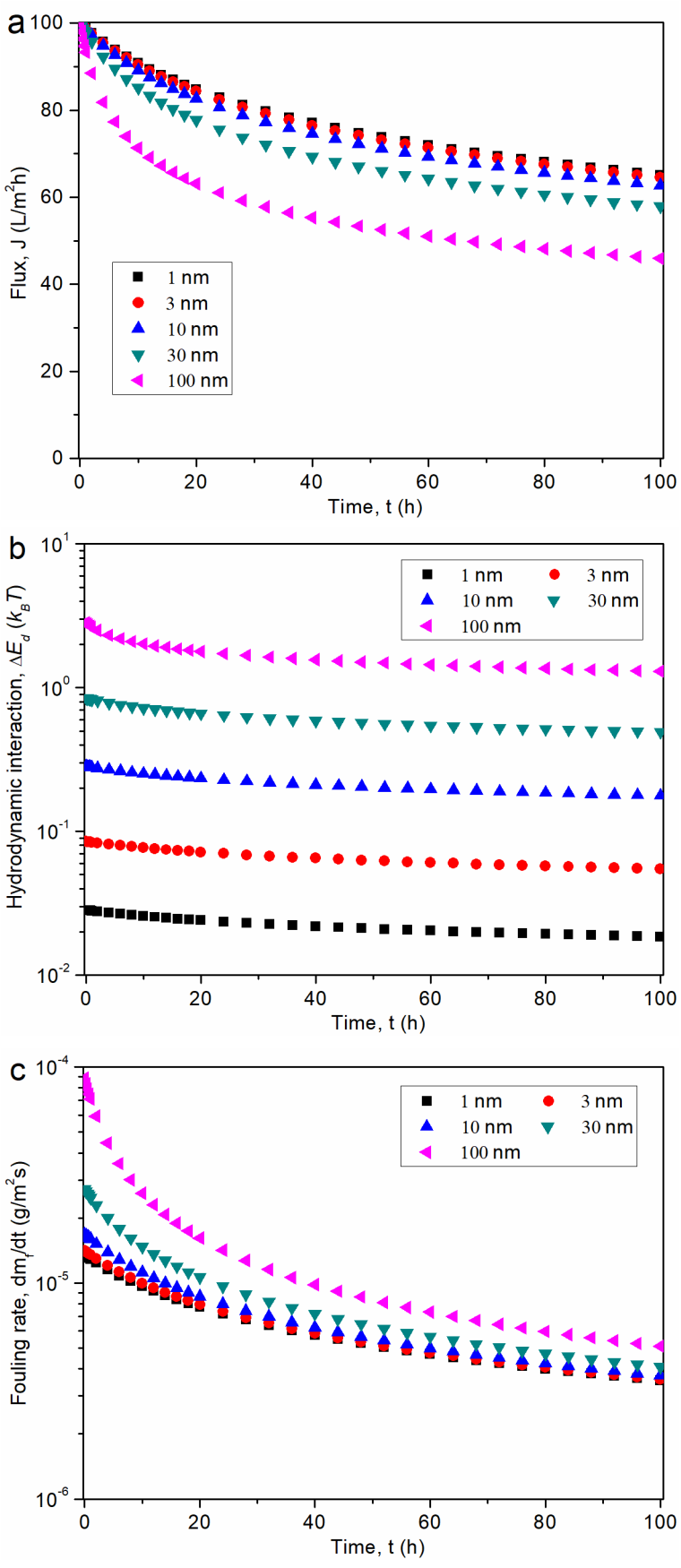

Fig. 5 Effect of colloidal particle size on hydrodynamic interaction and fouling. The

dependence of ΔE_d on d_p is determined by Eq. 16, and an empirical coefficient c_d of 4.19×10^{-9} is adopted. The values of α_f, D, k_m, and ΔE_b are fixed at 1.13×10^{13} m/g, 4.91×10^{-11} m^2/s, 1.02×10^{-5} m/s, and 5 k_BT, respectively. See other parameters in Table 1.

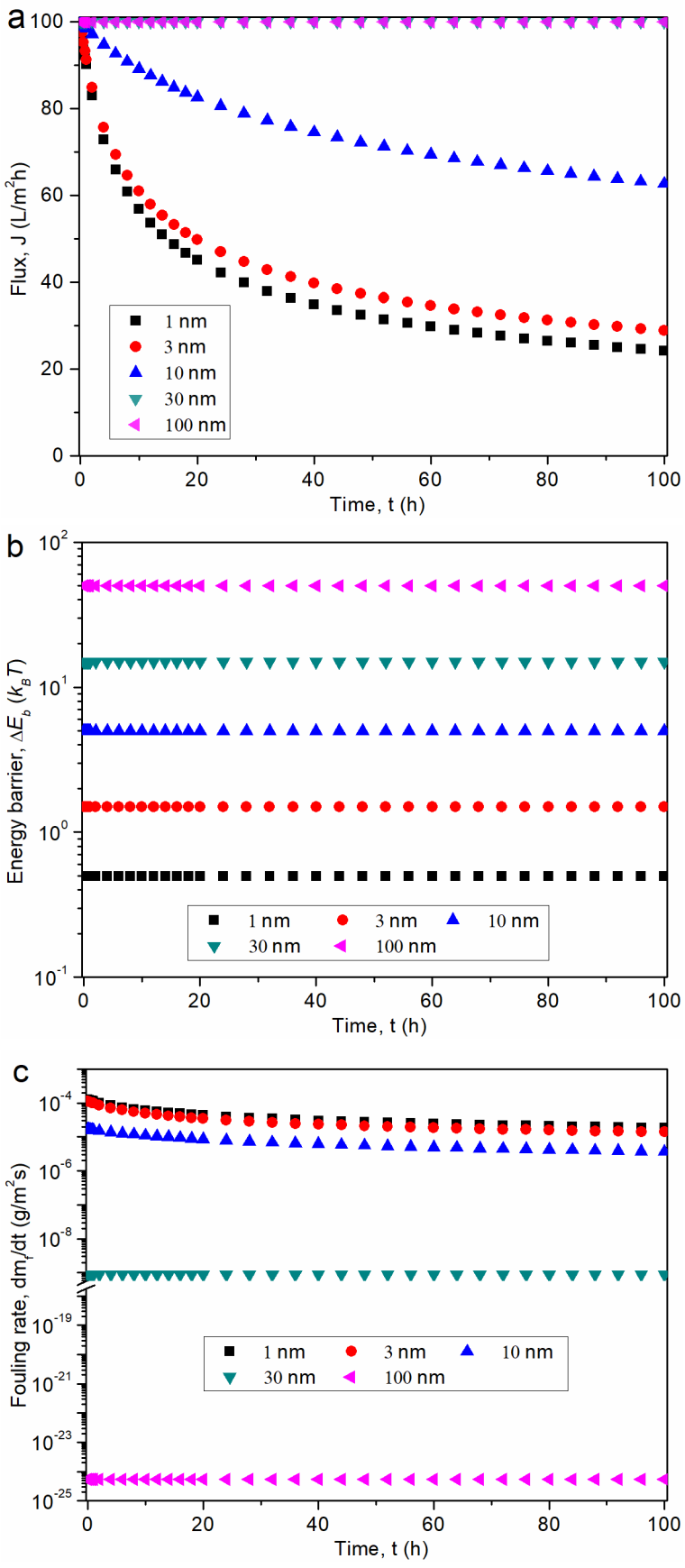

Fig. 6 Effect of colloidal particle size on foulant-membrane interaction and fouling. The

dependence of ΔE_b on d_p is determined by Eq. 19, with a constant c_E of 0.5 adopted. The values of α_f, D, k_m, and ΔE_d are fixed at 1.13×10^{13} m/g, 4.91×10^{-11} m^2/s, 1.02×10^{-5} m/s, and $4.19 \times 10^{-17} \times J$, respectively. See other parameters in Table 1.

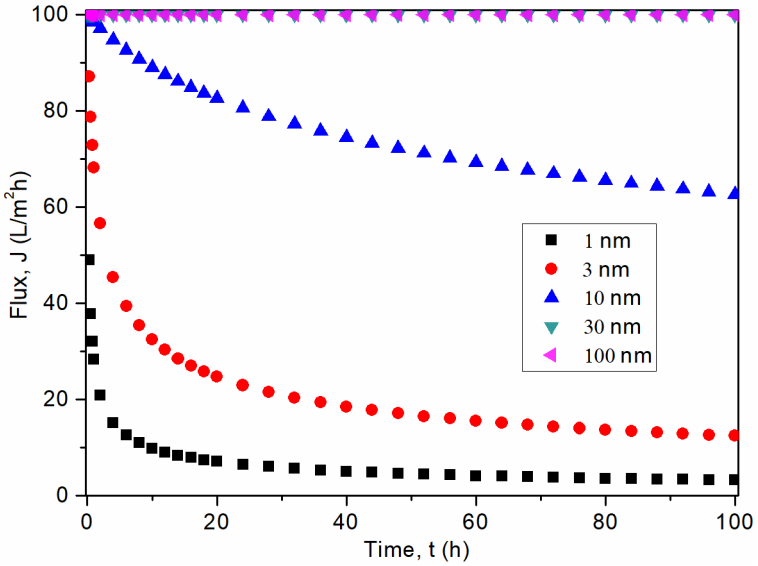

Fig. 7 Effect of colloidal particle size on fouling when all the four effects (i.e., specific cake resistance, back-diffusion, drag interaction and energy barrier) simultaneously change. The dependence of α_f, D, k_m, ΔE_d and ΔE_b on d_p are determined by Eq. 22, Eq. 15, Eq. 11, Eq. 16 and Eq. 19, respectively. See other parameters in Table 1.

169

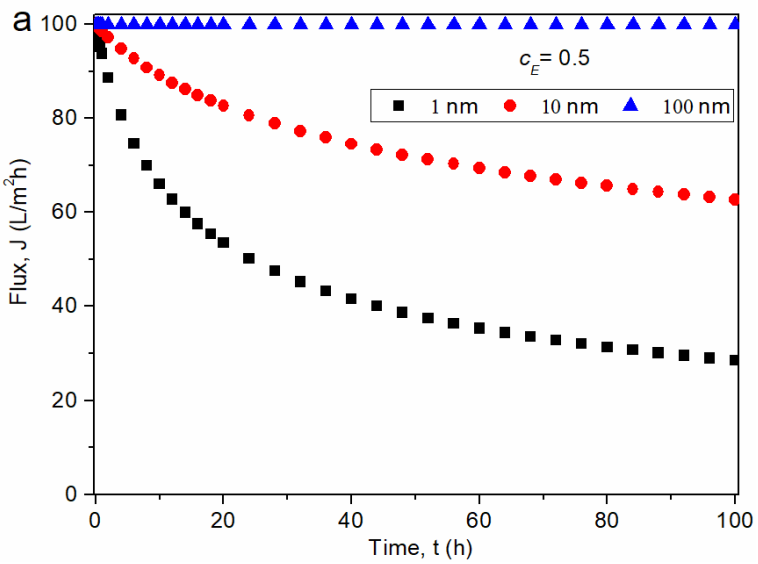

170

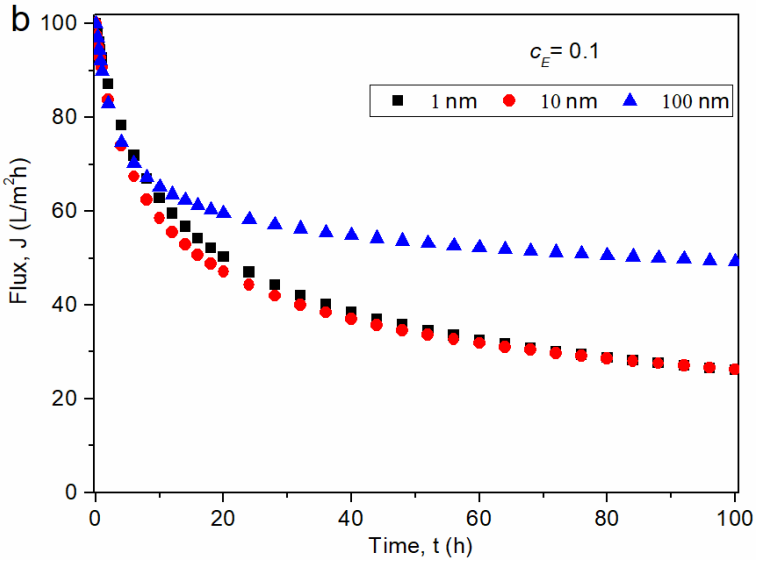

171

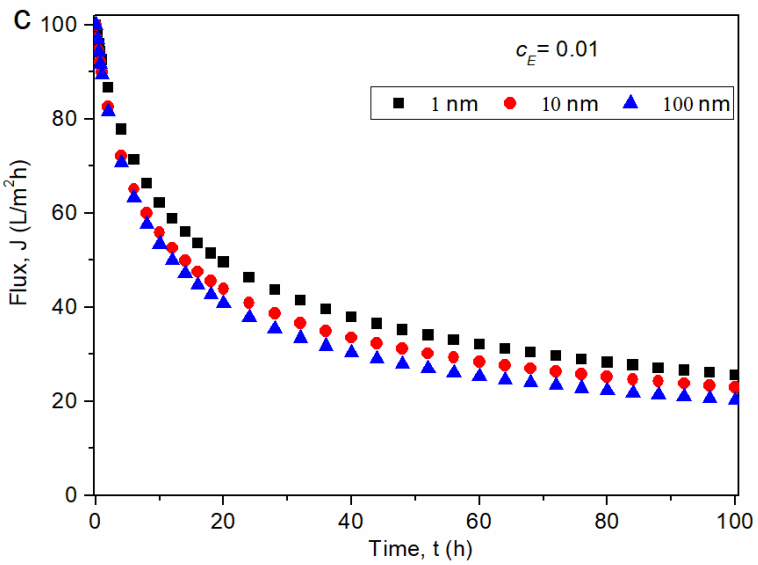

172

Fig. 8 Effect of colloidal particle size on fouling when the specific cake resistance is fixed (α_f = 1.13 × 10^{13} m/g) and the other three effects (i.e., back-diffusion, drag interaction and energy barrier) simultaneously change. The proportionality coefficient c_E for the energy barrier is taken as (a) 0.5, (b) 0.1, and (c) 0.01. The dependence of D, k_m, ΔE_d and ΔE_b on d_p are determined by Eq. 15, Eq. 11, Eq. 16 and Eq. 19, respectively. See other parameters in Table 1.

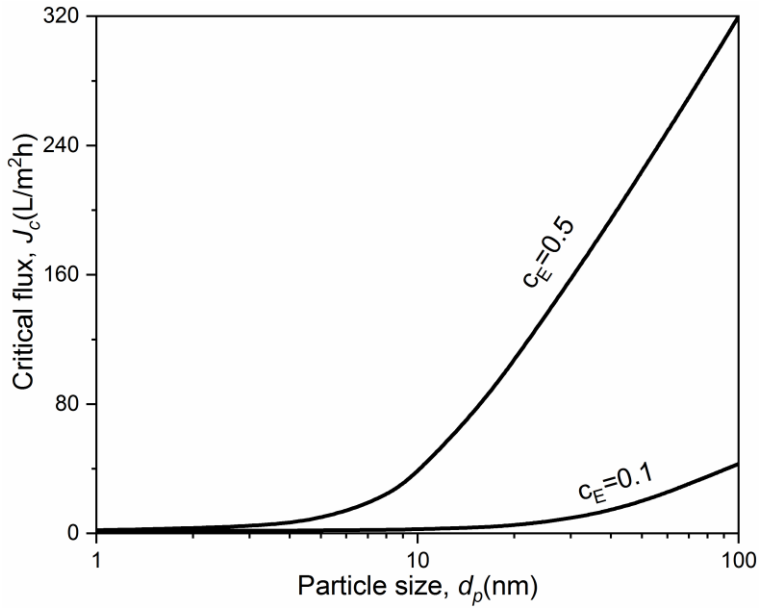

Fig. 9 Effect of particle size on critical flux at c_E = 0.5 and 0.1. A threshold fouling rate of 1.0 μg/(m^2·s) is adopted. The specific cake resistance is fixed (α_f = 1.13 × 10^{13} m/g) and the other three effects (i.e., back-diffusion, drag interaction and energy barrier) are allowed to change simultaneously. The dependence of D, k_m, ΔE_d and ΔE_b on d_p are determined by Eq. 15, Eq. 11, Eq. 16 and Eq. 19, respectively. See other parameters in Table 1.

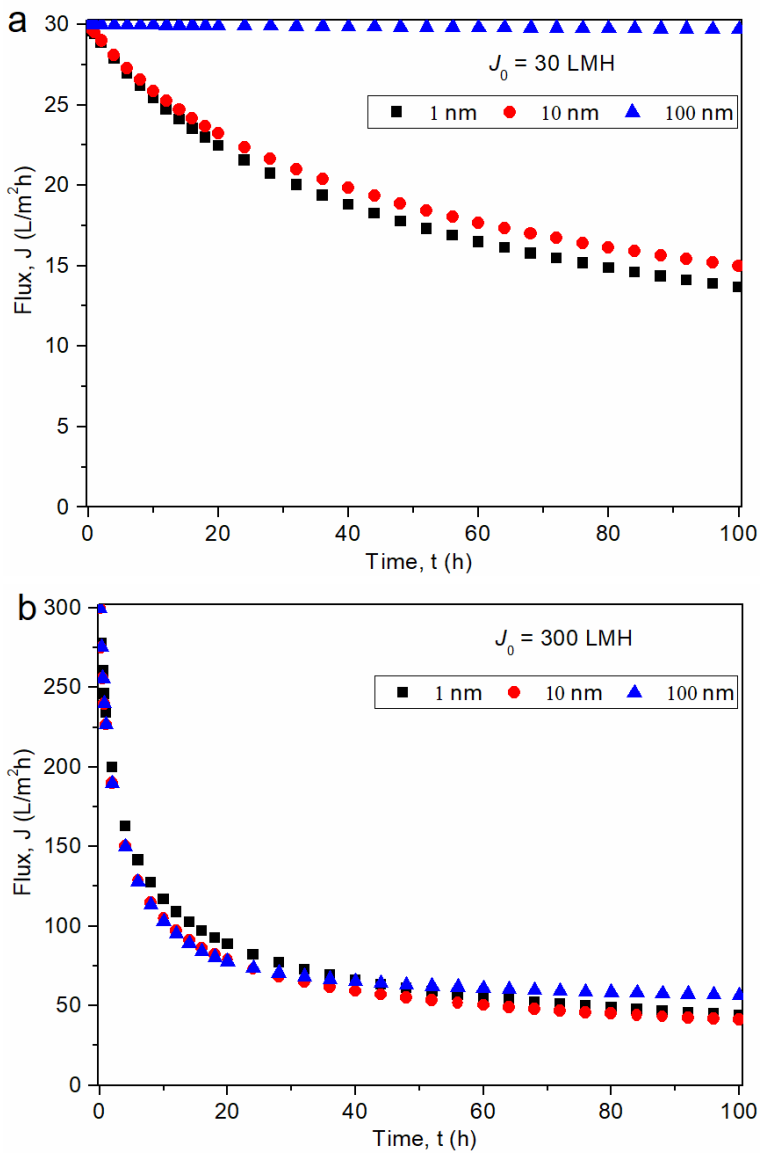

Fig. 10 Effect of colloidal particle size on fouling at initial flux of (a) 30 and (b) 300 LMH. The specific cake resistance is fixed (α_f = 1.13 × 10^{13} m/g) and the other three effects (i.e., back-diffusion, drag interaction and energy barrier) simultaneously change. A moderate foulant-membrane interaction is assumed (c_E = 0.1). The dependence of D, k_m, ΔE_d and ΔE_b on d_p are determined by Eq. 15, Eq. 11, Eq. 16 and Eq. 19, respectively. The other parameters are presented in Table 1.

Declaration of interests

☒The authors declare that they have no known competing financial interests or personal relationships that could have appeared to influence the work reported in this paper.

☐The authors declare the following financial interests/personal relationships which may be considered as potential competing interests:

CRediT authorship contribution statement

Junxia Liu: Conceptualization, Formal analysis, Methodology, Writing - Original Draft. **Yaxiang Zhao**: Software, Investigation. **Yaqian Fan**: Resources, Investigation. **Haiyan Yang**: Conceptualization, Writing - Review & Editing. **Zhihong Wang**: Project administration, Writing- Reviewing and Editing, Funding acquisition. **Yiliang Chen**: Writing - Review & Editing. **Chuyang Y. Tang**: Conceptualization, Methodology, Writing - Review & Editing.

Dissect the role of particle size through collision-attachment simulations for colloidal fouling of RO/NF membranes

Junxia Liu [a], Yaxiang Zhao [a], Yaqian Fan [a], Haiyan Yang [b], Zhihong Wang [a, *], Yiliang Chen [c], Chuyang Y. Tang [d, **]

[a] School of Civil and Transportation Engineering, Guangdong University of Technology, Guangzhou 510006, China

[b] SCNU Environmental Research Institute, Guangdong Provincial Key Laboratory of Chemical Pollution and Environmental Safety & MOE Key Laboratory of Theoretical Chemistry of Environment, South China Normal University, Guangzhou 510006, China

[c] College of Biology and the Environment, Nanjing Forestry University, Nanjing 210037, China

[d] Department of Civil Engineering, The University of Hong Kong, Pokfulam, Hong Kong SAR, China

*Corresponding author:

Zhihong Wang, gdutwzhrg@163.com;

Address: School of Civil and Transportation Engineering, Guangdong University of Technology, Guangzhou 510006, China

**Corresponding author:

Chuyang Y. Tang, tangc@hku.hk.

Address: Department of Civil Engineering, The University of Hong Kong, Pokfulam, Hong Kong SAR, China

Abstract

Colloidal size affects the whole process of particle transport and membrane filtration. However, its compound effect on fouling remains controversial. In the present study, we adopt a collision-attachment approach to systematically investigate the role of colloidal size on fouling. Our study highlights the critical importance of four competing mechanisms: reduced specific cake resistance and enhanced foulant-membrane interaction of larger particles tend to mitigate flux decline, while the simultaneously increased hydrodynamic drag and reduced particle back-transport tend to promote fouling. The net effect of particle size on fouling is governed by the competition among these mechanisms. When strong foulant-membrane repulsion prevails, we show enhanced flux stability for larger particles as a result of a greatly increased energy barrier to resist particle deposition. Nevertheless, this trend could be reversed for weak foulant-membrane interaction. Our study reconciles the contradictory experimental observations of the effect of particle size on colloidal fouling and provide important insights for effective fouling mitigation.

Keywords

Colloidal size, specific cake resistance, back-diffusion, hydrodynamic drag interaction, foulant-membrane interaction

1 Introduction

Nanofiltration (NF) and reverse osmosis (RO) have been increasingly applied in advanced water treatment over the past decades [1-3]. However, fouling presents a critical obstacle in these membrane processes [4-6]. Colloidal fouling is considered as one of the major types of fouling for both RO and NF. In addition to inorganic colloids, many common organic foulants such as humic acid, proteins, and polysaccharides also show colloidal characteristics [4, 7-9]. According to the literature, fouling behaviors of both inorganic and organic colloids are significantly influenced by their colloidal properties [4, 10, 11] in addition to the membrane properties [4, 7, 12], solution chemistry [8, 13], and hydrodynamic conditions [13, 14].

One of the most important colloidal properties is the particle size [11, 15-19]. Despite its fundamental importance, contradictory observations are often reported for the effect of colloidal size on fouling. Several studies revealed greater contribution to fouling by macromolecules of greater size [11, 15, 16]. Nevertheless, many other studies reported the dominant role of smaller-size colloids [17-19]. Although the effect of particle size has been extensively studied in the context of microfiltration (MF) and ultrafiltration (UF), it is often interpreted in relation to pore blocking behaviors [19-23], which is not applicable to RO and NF membranes. Furthermore, compared to the wide range of particle sizes reported for MF and UF membranes, colloids involved in the fouling of spiral-wound NF and RO modules are generally smaller than 100 nm due to the use of

extensive pretreatment [24-26]. Therefore, a systematical study is still required to better understand the role of colloidal size on the fouling behavior of NF and RO membranes.

Based on the existing literature, the dynamics of membrane fouling is governed by the compounded effects of (1) particle transport towards the membrane due to the hydrodynamic drag force [8, 14, 27]; (2) particle back-diffusion owing to the Brownian motion, lateral migration and shear-induced diffusion [4, 28] (noting that the latter two effects are negligible for small colloids of < 100 nm and are thus not important for NF and RO colloidal fouling [4, 28-30]); and (3) particle-membrane surface interactions (e.g., Lifshitz-van der Waals (LW), acid-base (AB), and electrostatic (EL) interaction [31-33]). Presumably, the colloidal size can significantly affect the hydrodynamics interaction [29], surface interaction [16], and the back-diffusion process [29], thereby regulates the dynamics of colloidal fouling. Furthermore, colloidal size is expected to greatly affect the property of the foulant cake layer, with smaller size leading to higher specific cake resistance [34]. All these effects have to be considered systematically to gain deeper insights into the role of colloid size on fouling.

Herein we report a collision-attachment (CA) model [27] to simulate the fouling dynamics of NF and RO membranes. This model treats colloidal fouling as (1) a series of colloid-membrane collision events followed by (2) colloidal attachment onto the membrane (i.e., foulant deposition events) in a statistical manner [27] analogous to the classical treatment of colloidal coagulation [35, 36]. In particular, the probability of

87 successful attachment, i.e., the attachment coefficient, is modelled by the Boltzmann
88 distribution [27, 37], which explicitly accounts for the effects of particle back-migration
89 based on mass transfer considerations [38, 39], hydrodynamic drag interaction via the
90 Stokes' law [40], and foulant-membrane interaction via the XDLVO theory [33].
91 Furthermore, the Carmen-Kozeny equation [41] is used to account for the effect of
92 colloidal size on the specific cake resistance. For the first time, this study clarifies the
93 role of particle size on fouling from the aspects of specific cake resistance, particle
94 back-diffusion, permeate drag interaction, foulant-membrane interaction, both
95 individually and collectively. Unlike the deterministic results in the existing literatures,
96 this study dissects the role of particle size dialectically. Our simulation results provide
97 new insights into the comprehensive role of particle size on fouling.
98

99 ## 2 Theory

100 This section first introduces the collision-attachment model in Sec. 2.1. We then briefly
101 present the concentration polarization (CP) and mass transfer in Sec. 2.2, followed by
102 an introduction of hydrodynamics drag and foulant-membrane interactions in Sec. 2.3
103 and cake layer resistance in Sec. 2.4. Finally, the algorithm for the simulation is
104 provided in Sec. 2.5.
105

106 ### 2.1 Collision attachment theory

107 The collision-attachment approach has been traditionally applied to model particle-

particle attachment during coagulation [35, 36]. Tang and coworkers [27, 37, 42] recently adapted this approach to simulate colloidal fouling by considering a membrane as an infinitely large particle. In essence, the model treats colloidal fouling as a series of collision events whose subsequent attachments onto the membrane leads to foulant deposition. According to Liu et al. [27], the rate of foulant deposition onto the membrane, i.e., the fouling rate dm_f/dt, is given by the product of the collision frequency JC_m and the attachment coefficient α as:

$$\frac{dm_f}{dt} = \alpha J C_m \qquad (1)$$

where m_f is the amount of foulant deposition at time t, J is water flux, C_m is the foulant concentration near the membrane surface, and the term JC_m characterizes how frequently colloidal particles transport towards and collide with the membrane surface [13]. Under crossflow conditions, only a fraction of these colloidal particles will attach onto the membrane, with the attachment coefficient α representing the probability of successful foulant-attachment onto membrane for a given collision event. The value of α can be determined by the Boltzmann distribution [27]:

$$\alpha = \frac{1}{1 + \exp\left(\frac{\Delta E_b}{k_B T} - \frac{\Delta E_d}{k_B T}\right)} \qquad (2)$$

where k_B and T are the Boltzmann's constant and absolute temperature, respectively.

The term ΔE_b represents the energy barrier corresponding to the foulant-membrane interaction that resists colloidal attachment, ΔE_d represents the hydrodynamic drag interaction that promotes colloidal attachment, and ΔE_b - ΔE_d represents the net difference in energy between the unattached and attached states for the colloidal particle. Therefore, $\Delta E_b/k_BT$ and $\Delta E_d/k_BT$ stands for the normalized energy barrier in resisting fouling and the normalized hydrodynamic drag in promoting fouling, respectively [27].

2.2 CP and mass transfer

As shown in Fig. 1, foulants move towards the membrane under the permeate drag. The retention of the colloidal particles results in an increased foulant concentration near the membrane surface (C_m) in comparison to the bulk solution (C_b), a phenomenon named "concentration polarization" or CP [38]. For typical NF and RO membranes, colloidal particles can be nearly perfectly rejected, i.e., the foulant concentration in the permeate water (C_p) is nearly zero. Accordingly, C_m can be determined by a modified film theory that takes account of the depolarization effect due to colloidal particle deposition onto the membrane [27, 37]:

$$\frac{C_m - \alpha C_m}{C_b - \alpha C_m} = \exp\left(\frac{J}{k_m}\right) \quad (3)$$

In Eq. 3, k_m is the mass transfer coefficient, and the term J/k_m is the Péclet number (Pe) that characterizes the relative importance of the convective transport (J) over the

diffusive transport (k_m). Compared to the traditional CP model (e.g., $C_m/C_b=\exp(J/k_m)$) [38, 43], the additional term αC_m in Eq. 3 accounts for the loss of foulant from the feed solution due to their deposition onto the membrane, which serves as a sink to reduce the CP effect.

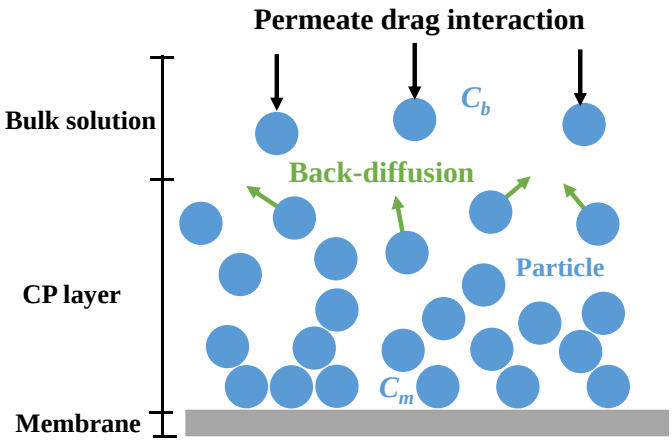

Fig. 1 CP and mass transfer during membrane filtration

By combing Eqs. 1-3, one can obtain

$$\frac{dm_f}{dt} = \gamma J C_b \tag{4a}$$

with

$$\gamma = \frac{1}{1 + \exp\left(\frac{\Delta E_b}{k_B T} - \frac{\Delta E_d}{k_B T} - \frac{J}{k_m}\right)} \tag{4b}$$

Eq. 4a relates the fouling rate dm_f/dt to the apparent collision frequency JC_b, in which the apparent attachment coefficient γ takes account of the CP effect on fouling [27, 37].

Correspondingly, the expression of γ (Eq. 4b) includes an additional term J/k_m in the exponent compared to that of the actual attachment coefficient α (Eq. 2).

Eq. 4b shows the critical role of CP and thus mass transfer near the membrane surface on colloidal fouling. Colloidal particles near the membrane surface can migrate back (i.e., back-diffusion) to the bulk solution (Fig. 1) due to Brownian motion, lateral migration (i.e., inertial lift) and shear-induced diffusion [4, 28, 30]. Among the three back-diffusion mechanisms, Brownian diffusion is the most important for small colloids (<< 1μm), whereas lateral migration and shear-induced diffusion are important for particles in the micrometer range [4, 28, 29]. Since spiral wound modules of NF and RO membranes are not designed to treat large sized particles, we only consider the effect of Brownian diffusion in this study (for colloidal sizes ranging from 1 to 100 nm). Accordingly, the mass transfer coefficient k_m in Eq. 4b is given by [39, 44]:

$$k_m = \frac{D}{\delta} \qquad (5)$$

where D and δ are the Brownian diffusion coefficient and Boundary layer thickness, respectively. The mass transfer coefficient k_m is often estimated according to the geometry of the fluid channel [39, 44]. In a spacer-filled channel, the relationship between mass transfer coefficient and Brownian diffusion coefficient is given by [39, 45, 46]:

$$k_m = Sh\frac{D}{d_h} \quad (6)$$

where d_h is the hydrodynamic diameter of the channel, and the dimensionless Sherwood number *Sh* represents the ratio of convective to diffusive mass transport [45, 47]. In the laminar flow regime, Sh in a rectangular flow channel can be determined by [45]:

$$Sh = 0.2\,Re^{0.57}\,Sc^{0.40} \quad (7)$$

where the Reynolds number *Re* and Schmidt number *Sc* are given by the following expressions, respectively:

$$Re = \frac{ud_h}{\nu} \quad (8)$$

$$Sc = \frac{\nu}{D} \quad (9)$$

where u is the crossflow velocity and ν is the kinematic viscosity (i.e., the ratio of viscosity μ of a fluid over its density ρ):

$$\nu = \frac{\mu}{\rho} \quad (10)$$

Substituting Eqs. 7-10 into Eq. 6, one can obtain

$$k_m = 0.2\frac{u^{0.57}\rho^{0.17}D^{0.6}}{\mu^{0.17}d_h^{0.43}} \quad (11)$$

Eq. 11 clearly shows that the mass transfer coefficient k_m is dependent on crossflow velocity u, fluid viscosity μ and density ρ, Brownian diffusion coefficient D, and hydrodynamic diameter d_h. Here the hydrodynamic diameter d_h is related to the geometry of the spacer and it can be generally defined by [39, 47, 48],

$$d_h = \frac{4\varepsilon_{sp}}{(2/h_{sp}) + (1-\varepsilon_{sp})S_{v,sp}} \quad (12)$$

where ε_{sp}, h_{sp} and $S_{v,sp}$ are the spacer porosity, the spacer thickness and the specific surface of the spacer, respectively.

For a rhombus type mesh spacer, the ε_{sp} and $S_{v,sp}$ can be determined by [39]

$$\varepsilon_{sp} = 1 - \frac{\pi d_{sp}^2}{2a_{sp}h_{sp}\,sin\,\theta_{sp}} \quad (13)$$

$$S_{v,sp} = \frac{4}{d_{sp}} \quad (14)$$

where d_{sp} is the spacer filament diameter, a_{sp} is the mesh size, and θ_{sp} is the angle between adjacent filaments.

The Brownian diffusion coefficient D is related to the particle size d_p by Stokes-Einstein relationship [38]:

$$D = \frac{k_B T}{3\pi\mu d_p} \tag{15}$$

The above mass transfer equations (Eqs. 11-15) in couple with CA theory (Eqs. 4a,b) can be implemented to model the role of colloidal size on Brownian diffusion coefficient, mass transfer coefficient and fouling.

2.3 Colloidal interactions

As shown in Fig. 2, particles transport towards membrane due to the permeate drag interaction, and those overcome the energy barrier ΔE_b of foulant-membrane interaction can successfully attach onto the membrane [4, 27, 40]. Therefore, the interplay of the hydrodynamic drag interaction and the foulant-membrane interaction plays a key role in regulating the particle deposition and thus the fouling behavior [8, 13, 14, 27, 37].

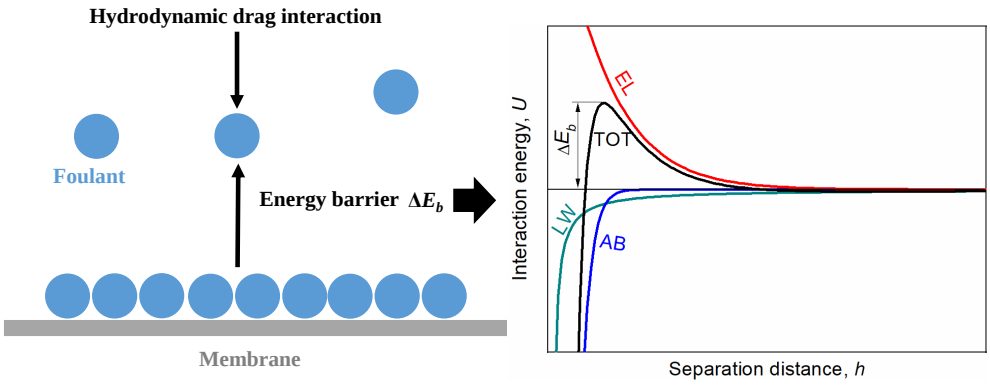

Fig. 2 Interactions acting on particles in colloidal attachment stage

The relationship between hydrodynamic drag interaction ΔE_d and colloidal particle size d_p can be expressed based on the Stokes law [40]:

$$\Delta E_d = 3\pi\mu d_p J \times l_d = c_d J d_p \quad (16)$$

where the term $3\pi\mu d_p J$ represents the permeate drag force on particle, l_d is the displacement of the particle relative to the fluid, and c_d is a proportionality coefficient characterizing the drag effect.

For the particle-membrane interaction, the particle size d_p can be related to the energy barrier ΔE_b via XDLVO theory [31-33]. According to XDLVO theory, the total interaction energy U^{TOT} for the foulant-membrane interaction is contributed by the Lifshitz-van der Waals interaction (U^{LW}), Acid-Base interaction (U^{AB}), and electrostatic interaction (U^{EL}):

$$U^{TOT}(h) = U^{LW}(h) + U^{AB}(h) + U^{EL}(h) \quad (17)$$

In Eq. 17, U^{TOT} is a function of the separation distance h between a colloid and membrane surface, and its maximum value can be taken as the energy barrier ΔE_b (see Fig. 2).

The LW, AB, and EL interactions in Eq. 17 can be further described by [33, 49-52]:

$$U^{LW}(h) = \pi \Delta G_{h_0}^{LW} \frac{h_0^2}{h} \times d_p \qquad (18a)$$

$$U^{AB}(h) = \pi \lambda \Delta G_{h_0}^{AB} \exp\left(\frac{h_0 - h}{\lambda}\right) \times d_p \qquad (18b)$$

$$U^{EL}(h) = \frac{\pi \varepsilon_r \varepsilon_0}{2}\left(2\zeta_f \zeta_m \ln\frac{1+\exp(-\kappa h)}{1-\exp(-\kappa h)} + \left(\zeta_f^2 + \zeta_m^2\right)\ln(1-\exp(-2\kappa h))\right) \times d_p \qquad (18c)$$

where h_0 is the minimum equilibrium separation distance (h_0 = 0.158 nm), and λ is the decay length of AB interaction in water (λ = 0.6 nm). In addition, $\Delta G_{h_0}^{LW}$ and $\Delta G_{h_0}^{AB}$ are the LW and AB energy per unit area at the separation distance of h_0, respectively. $\varepsilon_r \varepsilon_0$ is the dielectric permittivity of the solution; ζ_f and ζ_m are the zeta potentials of the foulant and the membrane, respectively; and κ is the inverse of the Debye screening length [4].

Eqs. 18a-18c clearly shows that all interaction energies, i.e., U^{LW}, U^{AB}, and U^{EL} are proportional to the colloidal size d_p. Therefore, the relationship between ΔE_b and d_p can be simplified by:

$$\Delta E_b = c_E d_p \qquad (19a)$$

With

$$c_E = \pi \Delta G_{h_0}^{LW} \frac{h_0^2}{h} + \pi \lambda \Delta G_{h_0}^{AB} \exp\left(\frac{h_0 - h}{\lambda}\right) + \frac{\pi \varepsilon_r \varepsilon_0}{2}\left(2\zeta_f \zeta_m \ln\frac{1+\exp(-\kappa h)}{1-\exp(-\kappa h)} + \left(\zeta_f^2 + \zeta_m^2\right)\ln(1-\exp(-2\kappa h))\right) \qquad (19b)$$

where c_E is the proportionality coefficient whose value is related to the membrane properties, colloidal characteristics, and solution chemistry.

Eq. 16 and Eq. 19 coupled with the CA theory can be used to simulate the effect of particle size on fouling from aspect of the drag interaction and foulant-membrane interaction, respectively.

2.4 Cake layer resistance

According to CA theory, when foulant particles come near the membrane surface, they will frequently collide with the membrane surface followed by their attachment [27, 37]. With more and more foulants attached to the membrane surface, a fouling cake layer is formed. This results in an additional hydraulic resistance, i.e., the cake resistance R_f, which decreases the membrane permeate flux under constant applied pressure. According to Darcy's law [53], the permeate flux during membrane filtration can be given by:

$$J = \frac{\Delta P}{\mu\left(R_m + R_f\right)} \qquad (20)$$

where ΔP is the applied pressure, μ is the solution viscosity, and R_m is membrane inherent resistance. The cake resistance R_f is further related to foulant mass deposition

m_f by specific cake resistance α_f:

$$R_f = \alpha_f m_f \quad (21)$$

It is widely accepted that the specific cake resistance α_f generally exerts important roles in membrane fouling [34, 54, 55]. α_f is very sensitive to the particle size d_p, and can be estimated from the Carmen–Kozeny equation [41]:

$$\alpha_f = \frac{180(1-\varepsilon_f)}{\rho_p \varepsilon_f^3 d_p^2} \quad (22)$$

where ε_f is the porosity of the cake layer, and ρ_p is the particle density. The above Carmen–Kozeny equation coupled with CA theory and the Darcy Law provides a framework to simulate the effect of colloidal size on fouling from the aspect of specific cake resistance.

2.5 Algorithm procedures

The model presented in Sections 2.1-2.4 can be implemented using a spreadsheet. The key parameters used for the simulation in the current study are listed in Table 1. The following algorithm procedures are applied in the simulation:

1. For any given particle size d_p, the value of mass transfer coefficient k_m, permeate drag interaction ΔE_d, energy barrier ΔE_b, and specific cake resistance α_f can be

calculated via Eq. 11, Eq. 16, Eq. 19, and Eq. 22, respectively.

2. Initial flux J_0 can be obtained from Eq. 20 using $(R_f)_0 = 0$ at constant applied pressure. Alternatively, if the initial value of J_0 is specified, Eq. 20 can be used to find the required pressure.
3. Once J_0 is known, Eq. 4b and Eq. 4a can be used to determine the initial value of attachment coefficient γ and fouling rate dm_f/dt, respectively.
4. The increment of foulant mass deposition Δm_f at each time step Δt can be estimated by $(dm_f/dt) \times \Delta t$.
5. With the new m_f value, Eq. 21, Eq. 20, Eq. 4b and Eq. 4a can be adopted to update R_f, J, γ and dm_f/dt, respectively.
6. Step 3 – 5 can be repeated to determine water flux J over time.

Table 1 Parameters for the simulation

	Parameters	Value	Remarks
Feed property	Particle size, d_p	1-100 nm	Note [a]
	Foulant concentration, C_b	5 mg/L	Ref. [14]
	Solution viscosity, μ	8.9×10^{-4} Pa·s	Ref. [27]
Operation conditions	Crossflow velocity, u	20 cm/s	Ref. [14]
	Absolute temperature, T	298.15 K	Ref. [27]
	Initial water flux, J_0	100 L/(m^2·h)	
	Membrane resistance, R_m	4.50×10^{13} m^{-1}	Ref. [27]
Cake property	Cake porosity, ε_f	0.4	Note [b]
	Particle density, ρ_p	1.5×10^6 g/m^3	Ref. [37]
	Specific cake resistance, α_f	$\frac{180(1-\varepsilon_f)}{\rho_p \varepsilon_f^3 d_p^2}$	Ref. [41]
Spacer Filaments	Spacer thickness, h_{sp}	1.15 mm	Ref. [27]
	Filament diameter, d_{sp}	0.60 mm	Ref. [27]
	Mesh size, a_{sp}	2.95 mm	Ref. [27]
	Filaments intersection angle, θ_{sp}	90°	Ref. [27]

Mass transfer	Diffusion coefficient, D	$\frac{k_B T}{3\pi\mu d_p}$	[38]
	Mass transfer coefficient, k_m	2.55×10^{-6} ~ 4.04×10^{-5}m/s	Note [c]
Colloidal Interaction	Unit energy, k_BT	4.11×10^{-21} J	
	Drag interaction, ΔE_d	$c_d J d_p$	Note [d]
	Energy barrier, ΔE_b	$c_E d_p$	Note [e]

Notes: [a]An approximate geometric sequence of dp=1, 3, 10, 30, 100 nm is adopted in the simulation, which allows us to investigate over a wide range of colloidal size. [b]A fixed porosity of 0.4 is adopted based on the reports of humic acid [56-58] [c]The value of mass transfer coefficient k_m is calculated according to the mass transfer considerations (Eqs. 11-15). [d]Hydrodynamic drag interaction is determined through Stokes law (Eq. 16) with an empirical coefficient c_d of 4.19×10^{-9} adopted [27]. [e]Energy barrier of foulant-membrane is calculated according to XDLVO theory (Eqs. 19a, b) with a constant c_E of 0.5 applied in present study based on our previous works [27, 42]. [f]The values of the main parameters are adopted according to our previous work on NF membrane fouled by humic acid [14, 27, 37].

3 Results and discussion

In the following sub-sections, we simulate the role of colloidal size (d_p = 1-100 nm) on fouling through its effect on specific cake resistance (Sec. 3.1), particle back-diffusion (Sec. 3.2), permeate drag interaction (Sec. 3.3), and foulant-membrane interaction (Sec. 3.4) individually. For example, in Sec. 3.1, only the specific cake resistance is allowed to vary with the colloidal size while keep all other effects (back-diffusion, permeate

drag interaction, and foulant-membrane interaction) at their respective reference values. In the current study, these reference values were calculated at a fixed particle size of 10 nm. This approach allows us to dissect the individual contribution by each competing mechanism. The combined effects of all mechanisms are then discussed in Sec. 3.5.

3.1 Effect of specific cake resistance

Fig. 3a exhibits variations of flux behavior for particle size ranging from 1 to 100 nm from the aspect of specific cake resistance. With an initial flux of 100 L/m^{2}h (LMH), flux decline is more severe for smaller particles. For instance, the flux for d_p = 1 nm reaches < 20 LMH at the end of 100-h filtration, while flux decline is nearly negligible for the case of d_p = 100 nm. This difference can be attributed to the much greater specific cake resistance for the smaller particles according to the Carmen-Kozeny equation (Eq. 22), resulting in faster built-up of cake resistance (Fig. 3b) despite of a slower foulant accumulation (Fig. 3c). This result is supported by experimental studies that cake layers formed by small colloids were generally denser with greater specific cake resistance [54, 55].

In this set of results, the shape of fouling rate curves (Fig. 3c) generally mirrors that of flux curves (Fig. 3a). With the same initial flux, both collision frequency (JC_b) and attachment coefficient (γ) are identical among the different particle sizes at the beginning of filtration, assuming that the back-transport of particles, the hydrodynamic drag, and foulant-membrane interactions are not affected by particle size. As fouling

progresses, the faster flux decline for smaller particles results in both reduced collision frequency as well as the attachment coefficient, such that particles of 1 nm size will have the lowest rate of mass deposition at a longer fouling duration (Fig. 3c). Nevertheless, the slower rate of mass deposition is overweighed by the effect of specific cake resistance, causing an overall more rapid flux decline for smaller particles. It is also worthwhile to note that, for cases with less stable water flux (e.g., d_p < 10 nm in Fig. 3a), the flux first experiences a rapid initial decline but becomes more stable at a longer time of filtration. This self-stabilization behavior, underpinned by the rapidly reduced foulant deposition rate (Fig. 3c), has been widely documented for experiments performed under constant pressure conditions [8, 13, 14].

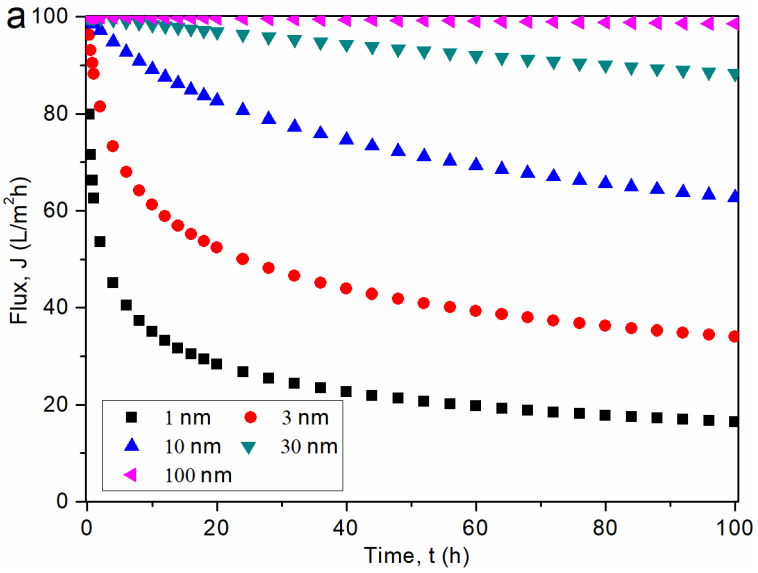

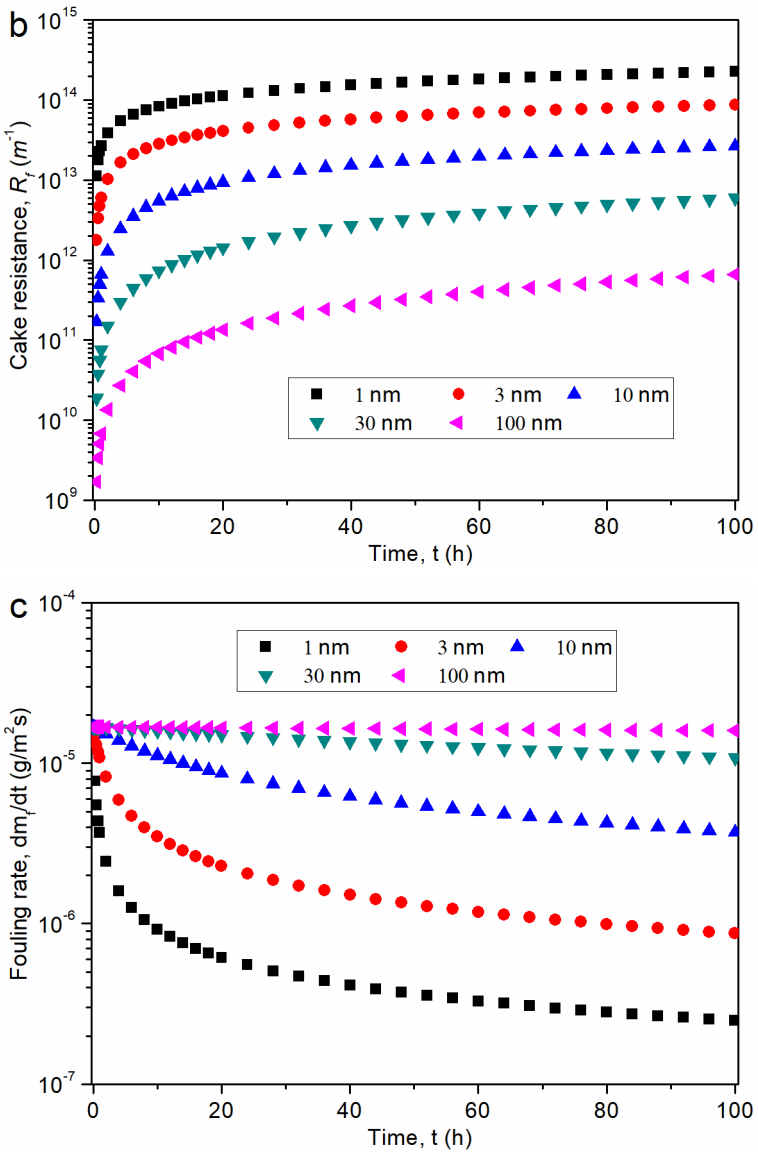

Fig. 3 Effect of colloidal particle size on fouling from the aspect of specific cake resistance. The dependence of α_f on d_p is determined according to Eq. 22. The value of D, k_m, ΔE_d and ΔE_b are fixed at 4.91×10^{-11} m^2/s, 1.02×10^{-5} m/s, $4.19 \times 10^{-17} \times J$ and $5k_BT$, respectively. See other parameters in Table 1.

3.2 Effect of particle back-transport

Fig. 4 presents the effect of particle size on fouling from the aspect of particle back-

diffusion. Contrary to the simulation results from the cake resistance aspect (Fig. 3a), larger colloidal size introduces a faster flux decline from the aspect of mass transfer coefficient (Fig. 4a). For example, the 100-nm colloids result in approximate 70% flux loss after 100 h filtration compared to approximately 15% loss for the 1-nm colloids over the same period. Fig. 4b presents the role of particle size on Peclet number (*Pe*), i.e., the ratio of permeate flux (J) to mass transfer coefficient (k_m). A larger *Pe* reflects a lower degree of diffusion compared convection and a more severe CP, and thus it is an important parameter for membrane fouling [5, 30]. At d_p = 1 nm, *Pe* is less than 1, revealing a low level of CP. *Pe* increases with the increasing colloidal size, which is attributed to the decreased Brownian diffusion coefficient (Eq. 15) and thus decreased mass transfer coefficient (Eq. 11). When colloidal size increases to 100 nm, *Pe* is larger than 10 at the beginning of filtration, inducing a high level of CP and therefore faster foulant mass deposition (Fig. 4c) and flux loss (Fig. 4a). Indeed, the shape of fouling rate curves (Fig. 4c) somewhat resembles that of the *Pe* curves (Fig. 4b) since the attachment coefficient γ is directly related to *Pe* (Eq. 4b). Our results highlight the key role of mass transfer on fouling, which echoes the existing literature on the importance of enhanced mass transfer (e.g., through spacer optimization) for fouling mitigation [39, 45, 46, 48].

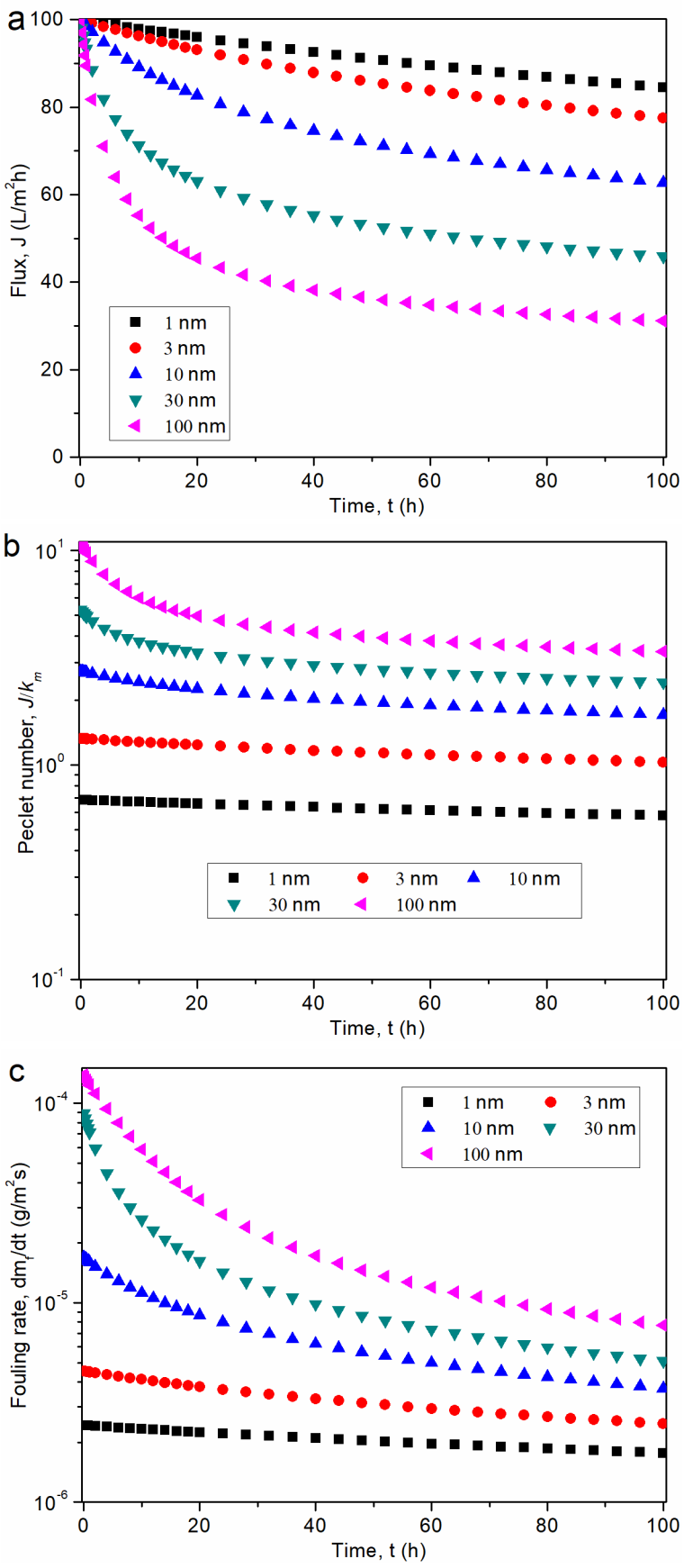

427

428

429

430 Fig. 4 Effect of colloidal particle size on fouling from the aspect of particle back-

diffusion and mass transfer coefficient. The dependence of D and k_m on d_p is determined according to Eq. 15 and Eq. 11, respectively. The value of α_f, ΔE_d and ΔE_b are fixed at 1.13×10^{13} m/g, $4.19 \times 10^{-17} \times J$ and $5k_BT$, respectively. See other parameters in Table 1.

3.3 Effect of hydrodynamic drag interaction

The simulation results are present in Fig. 5 for effect of particle size on fouling from the aspect of hydrodynamic interaction. Overall, more severe fouling happens with larger colloidal size. Specifically, for colloidal size of 1 nm with an initial flux of J_0=100 LMH, the flux decreases by approximately 30% after 100 h filtration (Fig. 5a). When the colloid size increases to 100 nm, the flux drops to half of the initial flux, indicating a more severe fouling. This more severe flux loss is due to the greater permeate drag interaction ΔE_d (Fig. 5b). Since the permeate drag force is directly proportional to the particle size according to the Stokes Law, the initial drag interaction ΔE_d for d_p=100 nm is two orders of magnitude larger than that for d_p=1 nm. This larger ΔE_d results in increased attachment coefficient γ (Eq. 2), which in turn promotes faster foulant mass deposition (Fig. 5c) and flux decline (Fig. 5a).

449

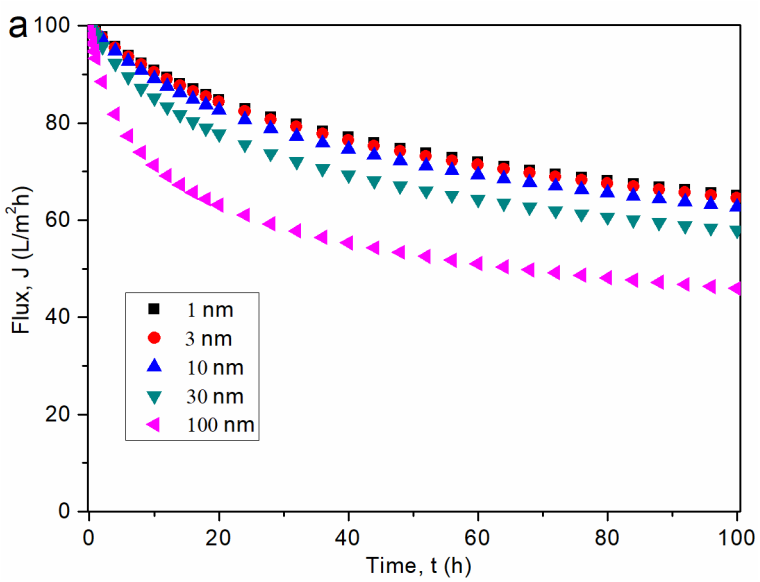

450

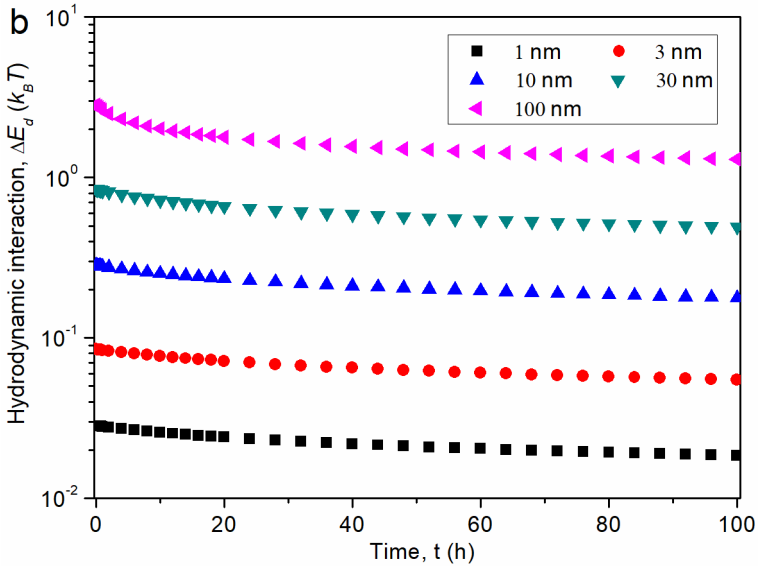

451

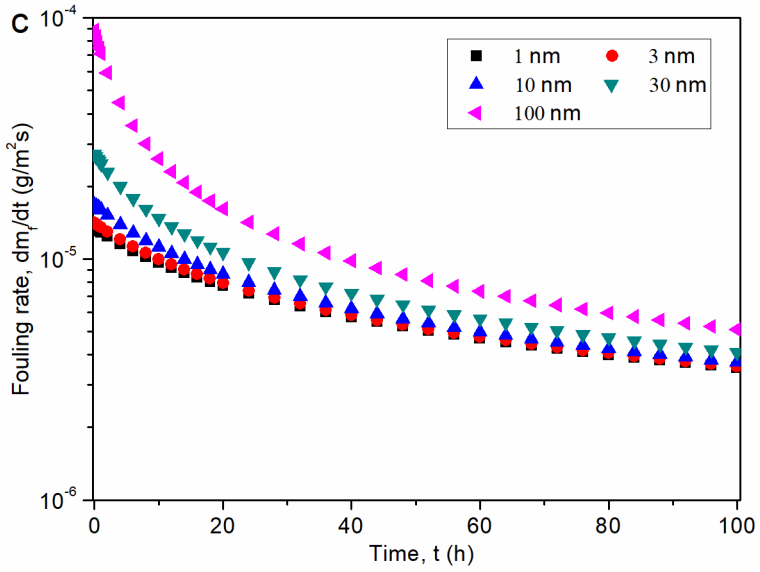

452 Fig. 5 Effect of colloidal particle size on hydrodynamic interaction and fouling. The

dependence of ΔE_d on d_p is determined by Eq. 16, and an empirical coefficient c_d of 4.19×10^{-9}[27] is adopted. The values of α_f, D, k_m, and ΔE_b are fixed at 1.13×10^{13} m/g, 4.91×10^{-11} m^2/s, 1.02×10^{-5} m/s, and 5 k_BT, respectively. See other parameters in Table 1.

3.4 Effect of foulant-membrane interaction

From the aspect of foulant-membrane interaction ΔE_b, much severe fouling occurs for the colloidal foulant with small-sized (i.e., d_p =1 and 3 nm, Fig. 6a), which is attributed to their weak energy barrier (Fig. 6b). Increased d_p from 3 nm to 10 nm can obviously alleviate fouling due to the substantially increased ΔE_b (Fig. 6b) and thus the decreased fouling rate by orders of magnitude (Fig. 6c). When the particle size increased to 30 nm or above, no obvious flux decline happens over the entire fouling duration of 100 h. Our simulation results indicate that the energy barrier ΔE_b is highly sensitive to the particle size, leading to a critical influence on the fouling rate and water flux decline. Our result supports the previous experimental reports that large-size colloidal foulants have more significant impact on colloid-surface interaction compared to the small-size ones [11, 16].

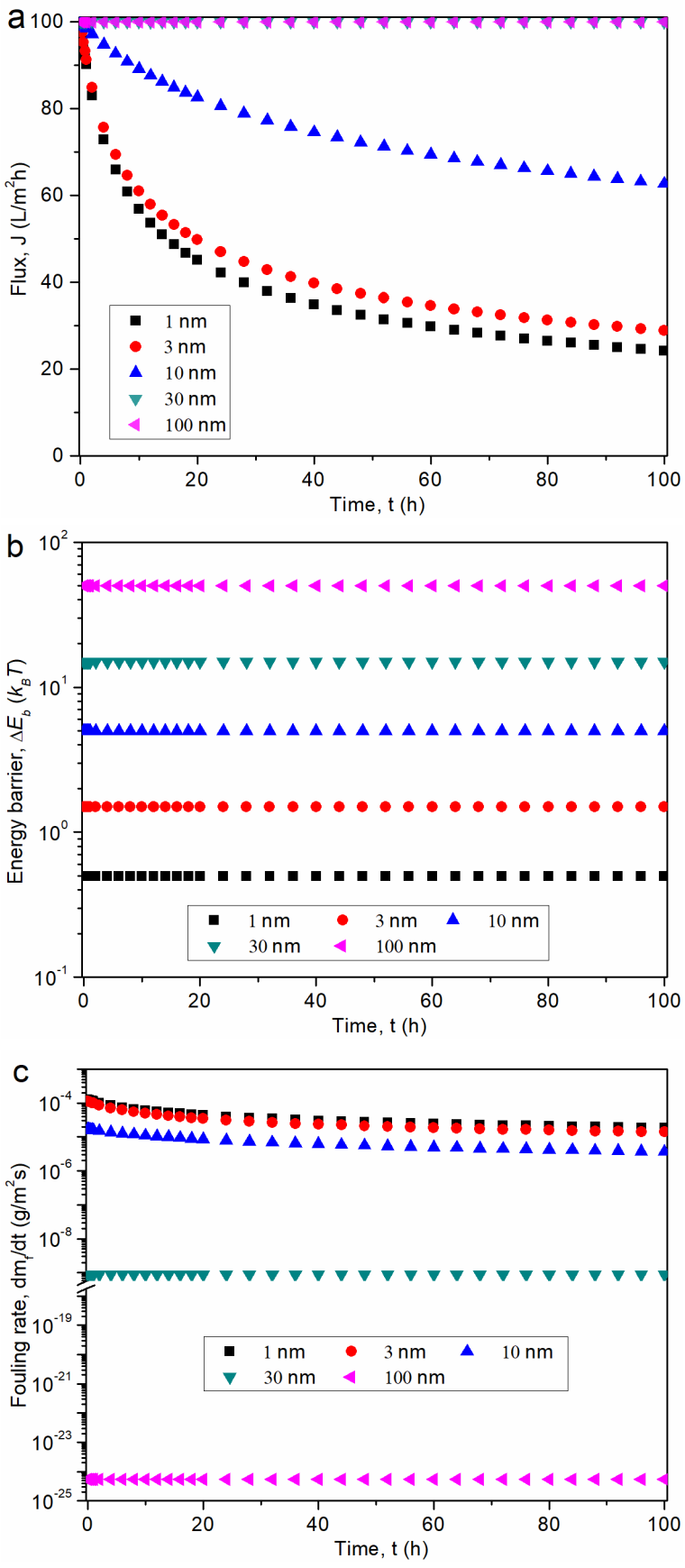

Fig. 6 Effect of colloidal particle size on foulant-membrane interaction and fouling. The

dependence of ΔE_b on d_p is determined by Eq. 19, with a constant c_E of 0.5 adopted. The values of α_f, D, k_m, and ΔE_d are fixed at 1.13×10^{13} m/g, 4.91×10^{-11} m^2/s, 1.02×10^{-5} m/s, and $4.19 \times 10^{-17} \times J$, respectively. See other parameters in Table 1.

In this series of simulation, no obvious flux decline happens when the particle size is larger than 30 nm (Fig. 6a). Such pseudo-stable flux behavior is consistent with the concept of critical flux [30, 59-61] (or limiting flux [14, 27, 40]): negligible fouling occurs if the flux is below a threshold value. It is important to note that the critical flux is strongly affected by foulant-membrane interaction [4, 14, 62]. Previously, Tang et al. [14, 40] proposed a simple conceptual model based on the principle of force balance (i.e. the hydrodynamic drag force balanced by the foulant-membrane interaction force) to interpret the existence of maximum pseudo-stable flux (i.e., the critical flux) during membrane filtration. The present study relates the pseudo-stable flux behavior to energy barrier via the effect of ΔE_b on the attachment coefficient γ (Eq. 4b). According to the XDLVO theory, the increased particle size (from 1-100 nm) can effectively increase the energy barrier of foulant-membrane (Fig. 6b), which provides strongly barrier preventing particle deposition. At a very high energy barrier, the attachment coefficient γ approaches to nearly zero, resulting in negligible foulant deposition (Fig. 6c).

3.5 Combined effect

In Sec.3.1-3.4, the effect of particle size on specific cake resistance, diffusion,

hydrodynamic drag interaction, and foulant-membrane interaction is individually assessed. Increasing particle size would decrease the specific cake resistance and increase the foulant-membrane interaction, both tend to mitigate membrane fouling. On the other hand, the reduced Brownian diffusion coefficient and increased hydrodynamic drag for larger particles tend to promote membrane fouling. Therefore, it is important to assess the combined effect of these competing mechanisms. Fig. 7 presents the dynamics of fouling as a function of particles size under the influence of all the four competing mechanisms following the simulation conditions specified in Table 1. Much severe fouling occurs with the smaller particle sizes (e.g., 1 and 3 nm), while fouling is milder for d_p = 10 nm and is nearly negligible for d_p = 30 nm and 100 nm. These results reveal the dominant role of specific cake resistance and foulant-membrane energy barrier compared to hydrodynamic drag interaction and Brownian diffusion (back-migration). Our study implies the critical role of the control of size particle, e.g., via pretreating the feed water to remove small particle fractions. In practice, the use of coagulation prior to membrane process has been shown to successfully mitigate colloidal fouling [63-65], which is consistent with our simulation results.

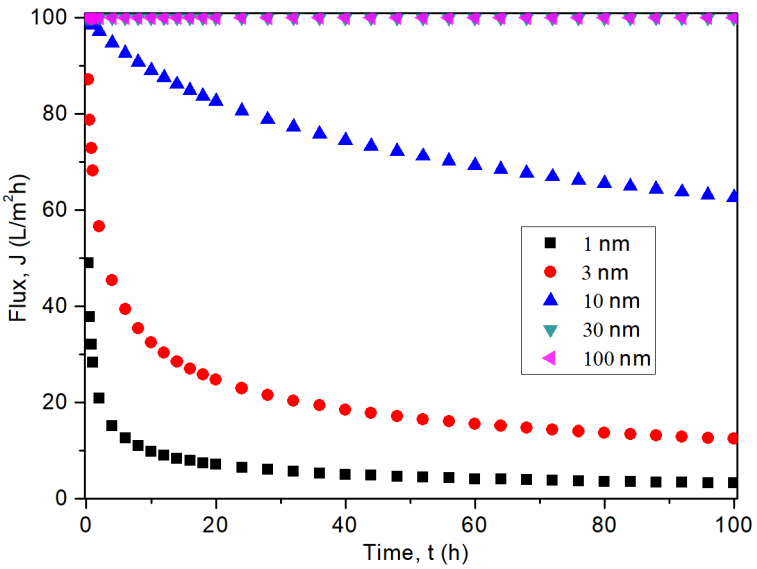

Fig. 7 Effect of colloidal particle size on fouling when all the four effects (i.e., specific cake resistance, back-diffusion, drag interaction and energy barrier) simultaneously change. The dependence of α_f, D, k_m, ΔE_d and ΔE_b on d_p are determined by Eq. 22, Eq. 15, Eq. 11, Eq. 16 and Eq. 19, respectively. See other parameters in Table 1.

It is important to note that the results in Fig. 7 assume that the specific cake layer resistance follows the Carmen–Kozeny equation (Eq. 22). In reality, the dependence of the specific cake layer resistance on particle size could be much weaker due to irregular packing of particles and non-spheric particles shapes. To provide additional insights into the governing mechanism(s) for colloidal fouling dynamics, we further simulated a case by fixing the specific cake layer resistance while allowing diffusion, hydrodynamic drag interaction, and foulant-membrane interaction to vary as a function of particle size. Despite the suppressed effect of the specific cake layer resistance, Fig. 8a still shows more severe fouling for smaller particles. The simulation results of Fig. 8a reveal the dominant role of foulant-membrane interaction in resistant colloidal

deposition on membranes. According to the XDLVO theory (Eq. 19a), the energy barrier resulting from colloid-membrane interaction is directly proportional to the colloidal size ($\Delta E_b = c_E\, d_p$, with a c_E value of 0.5 adopted as a reference value, see Table 1). Therefore, the 100-nm colloids offer much more repulsive interaction, i.e., greater ΔE_b value, compared to the 1-nm colloids, which dominates over the effect of back-diffusion and drag interaction and thus leads to a stable flux behavior.

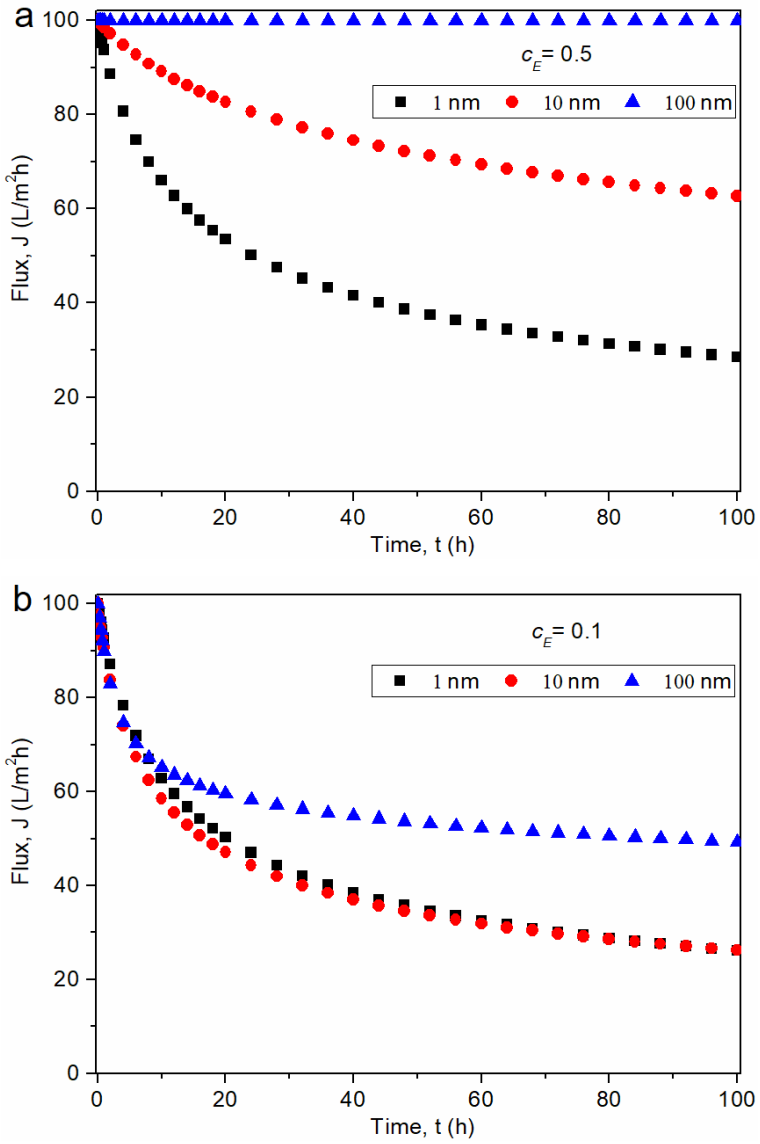

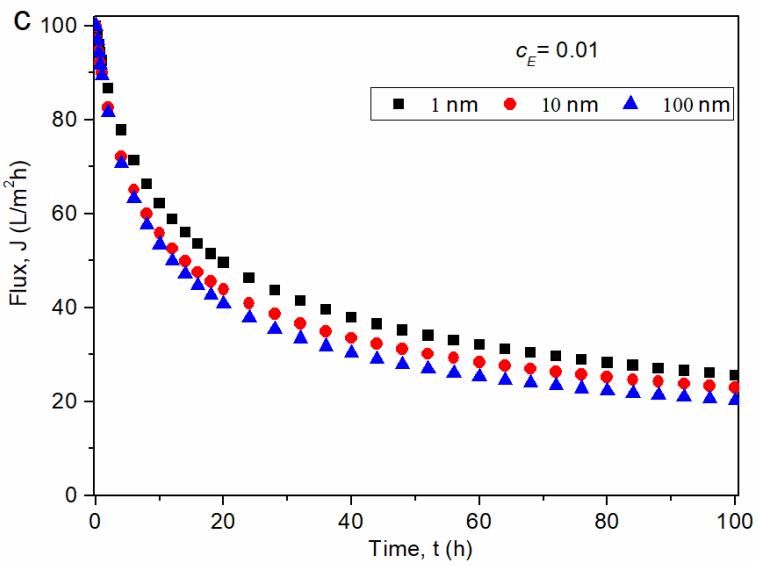

Fig. 8 Effect of colloidal particle size on fouling when the specific cake resistance is fixed (α_f = 1.13 × 10^{13} m/g) and the other three effects (i.e., back-diffusion, drag interaction and energy barrier) simultaneously change. The proportionality coefficient c_E for the energy barrier is taken as (a) 0.5, (b) 0.1, and (c) 0.01. The dependence of D, k_m, ΔE_d and ΔE_b on d_p are determined by Eq. 15, Eq. 11, Eq. 16 and Eq. 19, respectively. See other parameters in Table 1.

An important practical consideration is that the foulant-membrane interaction can be greatly affected by the solution chemistry. For example, the electrostatic repulsion between humic acid and a fouled membrane surface could be severely suppressed at lower solution pH, higher ionic strength, or with the addition of calcium in the solution, resulting in weakened foulant-membrane interaction [40, 66]. Similar effect of solution chemistry has also been reported for membrane fouling by alginate, proteins, and other charged foulants [8, 67, 68]. To cater for possible unfavorable solution chemistry, we also simulated cases of weaker foulant-membrane interaction by adopting smaller c_E

554 values (i.e., c_E = 0.1 in Fig. 8b and 0.01 in Fig. 8c). In general, the weakened energy
555 barrier, represented by smaller c_E values, leads to more severe flux loss, which is
556 consistent with numerous experimental observations [8, 13, 31, 40, 69]. However, the
557 larger particles are more severely affected by the reduced c_E value. At c_E = 0.1 (Fig. 8b),
558 particles of 1 nm and 10 nm show nearly identical flux decline curves, which indicate
559 that the effect of back-diffusion and drag interaction start to be as important as the effect
560 of foulant-membrane interaction. For an even weaker foulant-membrane interaction (c_E
561 = 0.01, Fig. 8c), the order of the three fouling curves is reversed, with larger particles
562 showing the greatest flux loss. Although this trend is completely opposite to the one
563 shown in Fig. 8a, the results can be reconciled considering the predominant effect of
564 drag interaction and back-diffusion when foulant-membrane interaction is severely
565 weakened. In this case, smaller particles are favored due to their greater Brownian
566 diffusion and smaller hydrodynamic drag force, both tend to reduce fouling.
567
568 In the classical review paper by Bacchin et al. [28], it was noted that particles in the
569 intermediate size range (d_p on the order of 100 nm) would be most prone to fouling,
570 with larger particles benefiting from shear-induced diffusion and lateral migration while
571 smaller particles favoring greater Brownian diffusion. In the current study, the effect of
572 shear-induced diffusion and lateral migration is not investigated since only particles of
573 100 nm or smaller are considered. The results in Fig. 8c are consistent with Bacchin et
574 al. [28] in that the greater Brownian diffusion of the smaller particles can lead to less
575 flux decline when the foulant-membrane interaction is negligible. However, this trend

may not be applicable when strong repulsive foulant-membrane interaction prevails. As predicted by Bacchin et al. [28] and many other studies [14, 37, 62], fouling behavior can be greatly affected by the foulant-membrane interaction. Indeed, our study shows that particles of 100 nm can have much stable water flux compared to particles of smaller sizes under moderate to strong foulant-membrane interaction (Fig. 8a,b). Although this trend appears to be counter-intuitive, it can be readily explained by the direct dependence of energy barrier on particle size.

In the field of membrane technology, a key milestone to comprehend the colloidal fouling is the concept of critical flux theory, which states that there is minimal flux decline when the operation flux is below a critical value [30, 59-61] (also see Sec. 3.4). According to the CA theory, the critical flux J_c can be operationally defined as the water flux with a very small fouling rate [42, 70]. To further reveal the role of colloidal size on membrane fouling, we plot the critical flux as a function of particle size under different c_E value using a threshold dm_f/dt of 1.0 μg/(m^2·s) [42] (Fig. 9). At c_E = 0.5, low J_c (< 40 LMH) is observed when particle size is less than 10 nm. However, increased particle size from 10 to 100 nm leads to substantially increased critical flux as a result of the dominate role of foulant-membrane interaction compared to the diffusion and drag interaction. With a d_p of 100 nm, the value of J_c is as high as 320 LMH. Our simulation reveals the critical role of particle size on critical flux. For a moderate c_E of 0.1, much lower critical flux is obtained (e.g., 43 LHM for d_p =100 nm) due to the weaker energy barrier. Our results highlight the importance of foulant-

membrane interaction (which is strongly affected by solution chemistry) on critical flux, which is consistent with the previous reports [14, 42, 70].

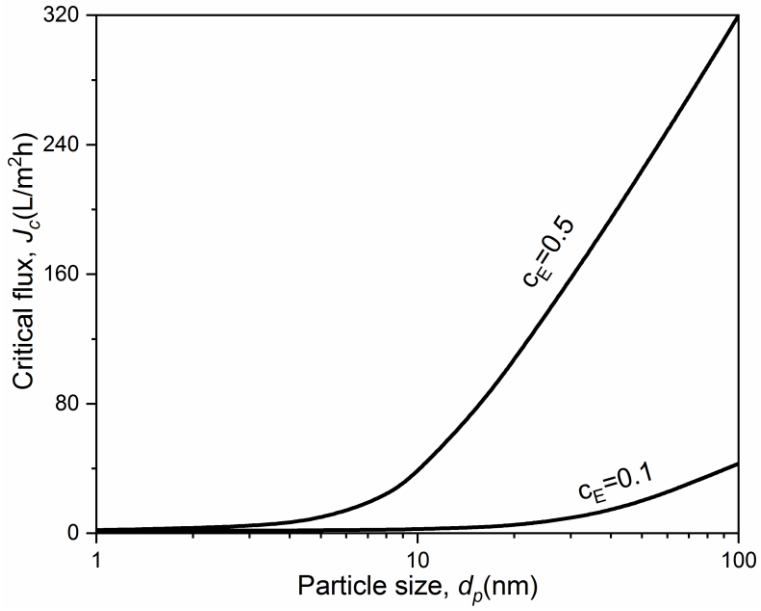

Fig. 9 Effect of particle size on critical flux at c_E = 0.5 and 0.1. A threshold fouling rate of 1.0 μg/(m^2·s) is adopted. The specific cake resistance is fixed (α_f = 1.13 × 10^{13} m/g) and the other three effects (i.e., back-diffusion, drag interaction and energy barrier) are allowed to change simultaneously. The dependence of D, k_m, ΔE_d and ΔE_b on d_p are determined by Eq. 15, Eq. 11, Eq. 16 and Eq. 19, respectively. See other parameters in Table 1.

The role of particle size on fouling is further complicated by the effect of the initial water flux. Fig. 10 presents simulations for additional initial fluxes of 30 LMH and 300 LMH for a moderate foulant-membrane interaction (c_E = 0.1). Although the effect of particle size was obvious for lower initial fluxes (30 LMH in Fig. 10a and 100 LMH in

Fig. 8b), it becomes less discernable for an initial flux of 300 LMH (Fig. 10b). While foulant-membrane interaction plays a dominant role in the former cases, the effect of permeate drag and concentration polarization become so severe at the initial flux of 300 LMH, which greatly destabilizes the 100-nm particles despite the existence of a large ΔE_b value.

The current study may provide important implications for membrane operation. In view of the severe fouling tendency under high membrane flux regardless of the particle size (Figure 10), elevated flux levels should be strictly avoided. In addition, adjustment of water chemistry may be considered to promote more repulsive foulant-membrane interactions to reduce fouling propensity. Under these conditions (strong foulant-membrane repulsion and low to moderate flux), the current study reveals more stable flux for larger particles. Our study underpins the effectiveness of pretreatment (e.g., water chemistry adjustment and coagulation) for effective fouling mitigation.

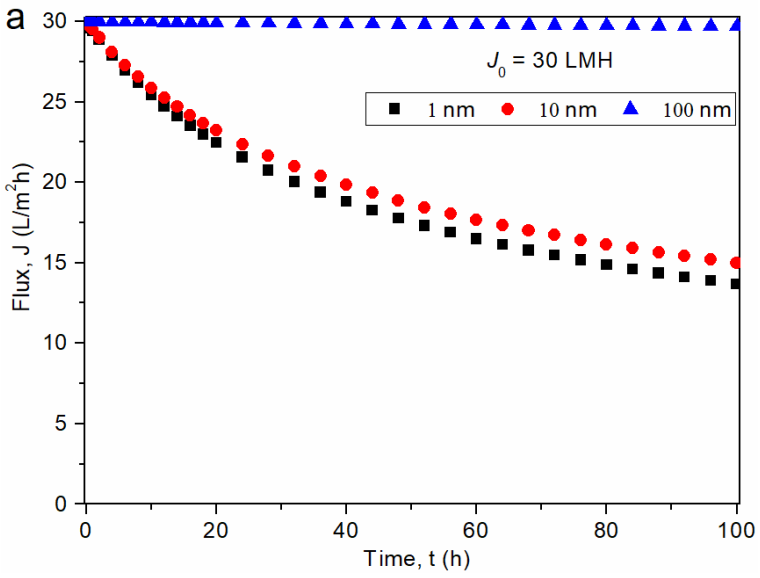

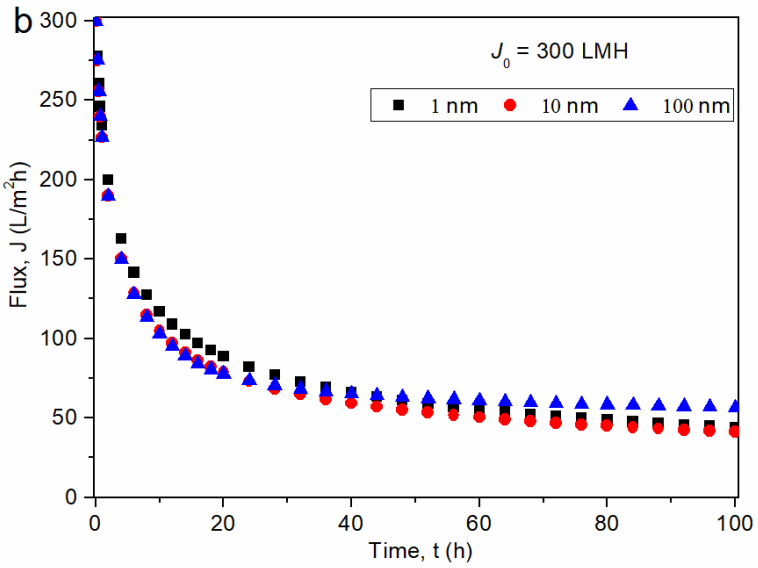

Fig. 10 Effect of colloidal particle size on fouling at initial flux of (a) 30 and (b) 300 LMH. The specific cake resistance is fixed (α_f = 1.13 × 10^{13} m/g) and the other three effects (i.e., back-diffusion, drag interaction and energy barrier) simultaneously change. A moderate foulant-membrane interaction is assumed (c_E = 0.1). The dependence of D, k_m, ΔE_d and ΔE_b on d_p are determined by Eq. 15, Eq. 11, Eq. 16 and Eq. 19, respectively. The other parameters are presented in Table 1.

4 Conclusion and implications

This study comprehensively explores the effects of particle size (d_p = 1-100 nm) on fouling dynamics. Larger particle size increases the hydrodynamic drag and reduces the Brownian diffusion, which tends to promote fouling. On the other hand, the reduced specific cake resistance and enhanced foulant-membrane interaction of larger particles tends to mitigate fouling. Therefore, the compound effect of particle size is a result of these competing mechanisms. Our study highlights a much more stable flux behavior

for the larger particles when strong foulant-membrane repulsion prevails even if the effect of specific cake resistance is ignored, which attributes to the strong dependence of the energy barrier on particle size. Nevertheless, the compound effect of particle size on flux decline can be weakened or even reversed for less repulsive foulant-membrane interaction. Our simulation results reconcile the contradictory experimental observations of the effect of particle size on colloidal fouling and provide important insights for developing strategies for fouling mitigation.

Our study may have important implications for mitigating colloidal fouling. In practical applications, the dominated mechanism for fouling is strongly affected by colloidal properties, membrane properties, solution chemistry, as well as operational conditions. For instance, membrane surface modification [2, 69, 71, 72] as well as water chemistry control [31, 42] can significantly enhance foulant-membrane energy barrier. Lower flux can be adopted to reduce CP and hydrodynamic drag [13, 14, 27], while spacer optimization can promote mass transfer with reduced CP [39, 45, 48]. Pretreatment of feedwater can also be adopted to not only control the distribution of particle size but also alter the properties of cake layer [65, 73, 74]. Future studies need to optimize fouling control strategies in accordance with the prevailing fouling mechanism(s).

Declaration of interests

The authors declare that they have no known competing financial interests or personal

relationships that could have appeared to influence the work reported in this paper.

CRediT authorship contribution statement

Junxia Liu: Conceptualization, Formal analysis, Methodology, Writing - Original Draft. **Yaxiang Zhao**: Software, Investigation. **Yaqian Fan**: Resources, Investigation. **Haiyan Yang**: Conceptualization, Writing - Review & Editing. **Zhihong Wang**: Project administration, Writing- Reviewing and Editing, Funding acquisition. **Yiliang Chen**: Writing - Review & Editing. **Chuyang Y. Tang**: Conceptualization, Methodology, Writing - Review & Editing.

Acknowledgements

This study was financially supported by the National Natural Science Foundation of China (51708130 and 51308131) and the Seed Fund for Basic Research by the University of Hong Kong (104005856).

References

[1] L.F. Greenlee, D.F. Lawler, B.D. Freeman, B. Marrot, P. Moulin, Reverse osmosis desalination: water sources, technology, and today's challenges, Water Res., 43 (2009) 2317-2348.

[2] C.Y. Tang, Z. Yang, H. Guo, J.J. Wen, L.D. Nghiem, E. Cornelissen, Potable Water Reuse through Advanced Membrane Technology, Environ. Sci. Technol., 52 (2018) 10215-10223.

[3] K.R. Zodrow, Q. Li, R.M. Buono, W. Chen, G. Daigger, L. Duenas-Osorio, M. Elimelech, X. Huang, G. Jiang, J.-H. Kim, B.E. Logan, D.L. Sedlak, P. Westerhoff,

689 P.J.J. Alvarez, Advanced Materials, Technologies, and Complex Systems
690 Analyses: Emerging Opportunities to Enhance Urban Water Security,
691 Environmental Science & Technology, 51 (2017) 10274-10281.
692 [4] C.Y. Tang, T. Chong, A.G. Fane, Colloidal interactions and fouling of NF and RO
693 membranes: a review, Adv. Colloid Interface Sci., 164 (2011) 126-143.
694 [5] P. Bacchin, A. Marty, P. Duru, M. Meireles, P. Aimar, Colloidal surface interactions
695 and membrane fouling: investigations at pore scale, Adv. Colloid Interface Sci.,
696 164 (2011) 2-11.
697 [6] X. Zhu, M. Elimelech, Colloidal Fouling of Reverse Osmosis Membranes:
698 Measurements and Fouling Mechanisms, Environ. Sci. Technol., 31 (1997) 736–
699 742.
700 [7] C.Y. Tang, Y.-N. Kwon, J.O. Leckie, Characterization of humic acid fouled reverse
701 osmosis and nanofiltration membranes by transmission electron microscopy and
702 streaming potential measurements, Environ. Sci. Technol., 41 (2007) 942-949.
703 [8] Y.-N. Wang, C.Y. Tang, Protein fouling of nanofiltration, reverse osmosis, and
704 ultrafiltration membranes—The role of hydrodynamic conditions, solution
705 chemistry, and membrane properties, J. Membr. Sci., 376 (2011) 275-282.
706 [9] Z. Xie, N. Nagaraja, L. Skillman, D. Li, G. Ho, Comparison of polysaccharide
707 fouling in forward osmosis and reverse osmosis separations, Desalination, 402
708 (2017) 174-184.
709 [10] J.A. Nilson, F.A. DiGiano, Influence of NOM composition on nanofiltration, J.
710 AWWA, 88 (1996) 53-66.
711 [11] Y. Tan, T. Lin, W. Chen, D. Zhou, Effect of organic molecular weight distribution
712 on membrane fouling in an ultrafiltration system with ozone oxidation from the
713 perspective of interaction energy, Environ. Sci.: Water Res. Technol., 3 (2017)
714 1132-1142.
715 [12] R. Li, Y. Lou, Y. Xu, G. Ma, B.Q. Liao, L. Shen, H. Lin, Effects of surface
716 morphology on alginate adhesion: Molecular insights into membrane fouling
717 based on XDLVO and DFT analysis, Chemosphere, 233 (2019) 373-380.
718 [13] Q. She, C.Y. Tang, Y.-N. Wang, Z. Zhang, The role of hydrodynamic conditions
719 and solution chemistry on protein fouling during ultrafiltration, Desalination, 249
720 (2009) 1079-1087.
721 [14] C.Y. Tang, J.O. Leckie, Membrane independent limiting flux for RO and NF
722 membranes fouled by humic acid, Environ. Sci. Technol., 41 (2007) 4767-4773.
723 [15] W. Sun, J. Nan, J. Xing, J. Tian, Influence and mechanism of different molecular
724 weight organic molecules in natural water on ultrafiltration membrane fouling
725 reversibility, RSC Advances, 6 (2016) 83456-83465.
726 [16] D. Zhao, J. Song, J. Xu, S. Yu, J. Liu, Y. Zhu, Z. Gu, G. Liu, Behaviours and
727 mechanisms of nanofiltration membrane fouling by anionic polyacrylamide with
728 different molecular weights in brackish wastewater desalination, Desalination, 468
729 (2019) 114058.
730 [17] M.R. Teixeira, V.S.O. Sousa, Fouling of nanofiltration membrane: Effects of NOM
731 molecular weight and microcystins, Desalination, 315 (2013) 149-155.
732 [18] C.-H. Yu, C.-H. Wu, C.-H. Lin, C.-H. Hsiao, C.-F. Lin, Hydrophobicity and

733 molecular weight of humic substances on ultrafiltration fouling and resistance, Sep.
734 Purif. Technol., 64 (2008) 206-212.
735 [19] J. Liu, Z. Wang, B. Dong, D. Zhao, Fouling behaviors correlating to water
736 characteristics during the ultrafiltration of micro-polluted water with and without
737 the addition of powdered activated carbon, Colloid Surface A, 511 (2016) 320-
738 328.
739 [20] M. Said, A. Ahmad, A.W. Mohammad, M.T.M. Nor, S.R. Sheikh Abdullah,
740 Blocking mechanism of PES membrane during ultrafiltration of POME, J. Ind.
741 Eng. Chem., 21 (2015) 182-188.
742 [21] K.J. Hwang, T.T. Lin, Effect of morphology of polymeric membrane on the
743 performance of cross-flow microfiltration, J. Membr. Sci., 199 (2002) 41-52.
744 [22] L. Li, Z. Wang, L.C. Rietveld, N. Gao, J. Hu, D. Yin, S. Yu, Comparison of the
745 effects of extracellular and intracellular organic matter extracted from Microcystis
746 aeruginosa on ultrafiltration membrane fouling: dynamics and mechanisms,
747 Environ. Sci. Technol., 48 (2014) 14549-14557.
748 [23] K. Gao, T. Li, J. Liu, B. Dong, H. Chu, Ultrafiltration membrane fouling
749 performance by mixtures with micromolecular and macromolecular organics,
750 Environ. Sci.: Water Res. Technol., 5 (2019) 277-286.
751 [24] M. Stoller, On the effect of flocculation as pretreatment process and particle size
752 distribution for membrane fouling reduction, Desalination, 240 (2009) 209-217.
753 [25] W.J. Lau, P.S. Goh, A.F. Ismail, S.O. Lai, Ultrafiltration as a pretreatment for
754 seawater desalination: A review, Membr. Water Treat., 5 (2014) 15-29.
755 [26] S.F. Anis, R. Hashaikeh, N. Hilal, Reverse osmosis pretreatment technologies and
756 future trends: A comprehensive review, Desalination, 452 (2019) 159-195.
757 [27] J. Liu, Z. Wang, C.Y. Tang, J.O. Leckie, Modeling Dynamics of Colloidal Fouling
758 of RO/NF Membranes with A Novel Collision-Attachment Approach, Environ.
759 Sci. Technol., 52 (2018) 1471-1478.
760 [28] P. Bacchin, P. Aimar, R.W. Field, Critical and sustainable fluxes: Theory,
761 experiments and applications, J. Membr. Sci., 281 (2006) 42-69.
762 [29] G. Belfort, R.H. Davis, A.L. Zydney, The behavior of suspensions and
763 macromolecular solutions in crossflow microfiltration, J. Membr. Sci., 96 (1994)
764 1-58.
765 [30] P. Bacchin, P. Aimar, V. Sanchez, Model for colloidal fouling of membranes,
766 AlChE J., 41 (1995) 368-376.
767 [31] Y. Ding, Y. Tian, Z. Li, H. Wang, L. Chen, Interaction energy evaluation of the role
768 of solution chemistry and organic foulant composition on polysaccharide fouling
769 of microfiltration membrane bioreactors, Chem. Eng. Sci., 104 (2013) 1028-1035.
770 [32] Z. Yin, Y. Ma, B. Tanis-Kanbur, W.C. Jia, Fouling behavior of colloidal particles
771 in organic solvent ultrafiltration, J. Membr. Sci., 599 (2020) 117836.
772 [33] J.A. Brant, A.E. Childress, Assessing short-range membrane–colloid interactions
773 using surface energetics, J. Membr. Sci., 203 (2002) 257-273.
774 [34] J. Teng, L. Shen, Y. Xu, Y. Chen, X.-L. Wu, Y. He, J. Chen, H. Lin, Effects of
775 molecular weight distribution of soluble microbial products (SMPs) on membrane
776 fouling in a membrane bioreactor (MBR): Novel mechanistic insights,

Chemosphere, 248 (2020) 126013.
[35] I.A. Valioulis, E.J. List, Collision efficiencies of diffusing spherical particles: hydrodynamic, van der Waals and electrostatic forces, Adv. Colloid Interface Sci., 20 (1984) 1-20.
[36] D. Thomas, S. Judd, N. Fawcett, Flocculation modelling: a review, Water Res., 33 (1999) 1579-1592.
[37] J. Liu, T. Huang, R. Ji, Z. Wang, C.Y. Tang, J.O. Leckie, Stochastic Collision-Attachment-Based Monte Carlo Simulation of Colloidal Fouling: Transition from Foulant-Clean-Membrane Interaction to Foulant-Fouled-Membrane Interaction, Environ. Sci. Technol., 54 (2020) 12703-12712.
[38] M.C. Porter, Concentration Polarization with Membrane Ultrafiltration, Ind Eng Chem Prod Res Dev, 11 (1972) 234-248.
[39] Q. She, D. Hou, J. Liu, K.H. Tan, C.Y. Tang, Effect of feed spacer induced membrane deformation on the performance of pressure retarded osmosis (PRO): Implications for PRO process operation, J. Membr. Sci., 445 (2013) 170-182.
[40] C.Y. Tang, Y.N. Kwon, J.O. Leckie, The role of foulant–foulant electrostatic interaction on limiting flux for RO and NF membranes during humic acid fouling—Theoretical basis, experimental evidence, and AFM interaction force measurement, J. Membr. Sci., 326 (2009) 526-532.
[41] P.C. Carman, Fluid flow through granular beds, Chem. Eng. Res. Des., 75 (1997) S32-S48.
[42] J. Liu, Y. Fan, Y. Sun, Z. Wang, D. Zhao, T. Li, B. Dong, C.Y. Tang, Modelling the critical roles of zeta potential and contact angle on colloidal fouling with a coupled XDLVO - collision attachment approach, J. Membr. Sci., 623 (2021) 119048.
[43] A.L. Zydney, C.K. Colton, A concentration polarization model for the filtrate flux in cross-flow microfiltration of particulate suspensions, Chem. Eng. Commun., 47 (1986) 1-21.
[44] E.M.V. Hoek, A.S. Kim, M. Elimelech, Influence of crossflow membrane filter geometry and shear rate on colloidal fouling in reverse osmosis and nanofiltration separations, Environ. Eng. Sci., 19 (2002) 357-372.
[45] C.P. Koutsou, S.G. Yiantsios, A.J. Karabelas, A numerical and experimental study of mass transfer in spacer-filled channels: Effects of spacer geometrical characteristics and Schmidt number, J. Membr. Sci., 326 (2009) 234-251.
[46] M. Shakaib, S.M.F. Hasani, M. Mahmood, CFD modeling for flow and mass transfer in spacer-obstructed membrane feed channels, J. Membr. Sci., 326 (2009) 270-284.
[47] G. Schock, A. Miquel, Mass transfer and pressure loss in spiral wound modules, Desalination, 64 (1987) 339-352.
[48] A.R. Da Costa, A.G. Fane, D.E. Wiley, Spacer characterization and pressure drop modelling in spacer-filled channels for ultrafiltration, J. Membr. Sci., 87 (1994) 79-98.
[49] J. Teng, L. Shen, Y. He, B.-Q. Liao, G. Wu, H. Lin, Novel insights into membrane fouling in a membrane bioreactor: Elucidating interfacial interactions with real membrane surface, Chemosphere, 210 (2018) 769-778.

821 [50] X. Cai, M. Zhang, L. Yang, H. Lin, X. Wu, Y. He, L. Shen, Quantification of
822 interfacial interactions between a rough sludge floc and membrane surface in a
823 membrane bioreactor, J. Colloid Interface Sci., 490 (2017) 710-718.
824 [51] J. Teng, M. Zhang, K.-T. Leung, J. Chen, H. Hong, H. Lin, B.-Q. Liao, A unified
825 thermodynamic mechanism underlying fouling behaviors of soluble microbial
826 products (SMPs) in a membrane bioreactor, Water Res., 149 (2019) 477-487.
827 [52] Y. Chen, L. Shen, R. Li, X. Xu, H. Hong, H. Lin, J. Chen, Quantification of
828 interfacial energies associated with membrane fouling in a membrane bioreactor
829 by using BP and GRNN artificial neural networks, J. Colloid Interface Sci., 565
830 (2020) 1-10.
831 [53] S. Hong, M. Elimelech, Chemical and physical aspects of natural organic matter
832 (NOM) fouling of nanofiltration membranes, J. Membr. Sci., 132 (1997) 159-181.
833 [54] F. Meng, H. Zhang, F. Yang, L. Liu, Characterization of Cake Layer in Submerged
834 Membrane Bioreactor, Environ. Sci. Technol., 41 (2007) 4065-4070.
835 [55] H.J. Lin, W.J. Gao, K.T. Leung, B.Q. Liao, Characteristics of different fractions of
836 microbial flocs and their role in membrane fouling, Water Sci. Technol., 63 (2011)
837 262-269.
838 [56] Y. Wei, A. Kocic, A.L. Zydney, Analysis of humic acid fouling during
839 microfiltration using a pore blockage-cake filtration model, J. Membr. Sci., 198
840 (2002) 51-62.
841 [57] Q. Li, M. Elimelech, Synergistic effects in combined fouling of a loose
842 nanofiltration membrane by colloidal materials and natural organic matter, J.
843 Membr. Sci., 278 (2006) 72-82.
844 [58] C. Zhao, T. Song, Y. Yu, L. Qu, J. Cheng, W. Zhu, Q. Wang, P. Li, W. Tang, Insight
845 into the influence of humic acid and sodium alginate fractions on membrane
846 fouling in coagulation-ultrafiltration combined system, Environ. Res., 191 (2020)
847 110228.
848 [59] R. Field, D. Wu, J. Howell, B. Gupta, Critical flux concept for microfiltration
849 fouling, J. Membr. Sci., 100 (1995) 259-272.
850 [60] R.W. Field, G.K. Pearce, Critical, sustainable and threshold fluxes for membrane
851 filtration with water industry applications, Adv. Colloid Interface Sci., 164 (2011)
852 38-44.
853 [61] T. Nguyen, C. Lee, R. Field, I. Kim, Insight into organic fouling behavior in
854 polyamide thin-film composite forward osmosis membrane: Critical flux and its
855 impact on the economics of water reclamation, J. Membr. Sci., 606 (2020) 118118.
856 [62] L. Shan, H. Fan, H. Guo, S. Ji, G. Zhang, Natural organic matter fouling behaviors
857 on superwetting nanofiltration membranes, Water Res., 93 (2016) 121-132.
858 [63] J. Kavitha, M. Rajalakshmi, A.R. Phani, M. Padaki, Pretreatment processes for
859 seawater reverse osmosis desalination systems—A review, J. Water Process Eng.,
860 32 (2019) 100926.
861 [64] B. Cyna, G. Chagneau, G. Bablon, N. Tanghe, Two years of nanofiltration at the
862 Méry-sur-Oise plant, France, Desalination, 147 (2002) 69-75.
863 [65] T.A. Malkoske, P.R. Bérubé, R.C. Andrews, Coagulation/flocculation prior to low
864 pressure membranes in drinking water treatment: a review, Environ. Sci.: Water

Res. Technol., 6 (2020) 2993-3023.
[66] C.Y. Tang, Y.-N. Kwon, J.O. Leckie, Fouling of reverse osmosis and nanofiltration membranes by humic acid—Effects of solution composition and hydrodynamic conditions, J. Membr. Sci., 290 (2007) 86-94.
[67] S. Lee, W.S. Ang, M. Elimelech, Fouling of reverse osmosis membranes by hydrophilic organic matter: implications for water reuse, Desalination, 187 (2006) 313-321.
[68] S. Lee, J. Cho, M. Elimelech, Influence of colloidal fouling and feed water recovery on salt rejection of RO and NF membranes, Desalination, 160 (2004) 1-12.
[69] Z. Arif, N. Sethy, L. Kumari, P. Mishra, B. Verma, Antifouling behaviour of PVDF/TiO2 composite membrane: a quantitative and qualitative assessment, Iran. Polym. J., 28 (2019) 301–312.
[70] J. Liu, Z. Wang, C.Y. Tang, J.O. Leckie, Modeling Dynamics of Colloidal Fouling of RO/NF Membranes with A Novel Collision-Attachment Approach, Environ. Sci. Technol., 52 (2018) 1471.
[71] X. Zhao, R. Zhang, Y. Liu, M. He, Y. Su, C. Gao, Z. Jiang, Antifouling membrane surface construction: Chemistry plays a critical role, J. Membr. Sci., 551 (2018) 145-171.
[72] Z. Yang, X.-H. Ma, C.Y. Tang, Recent development of novel membranes for desalination, Desalination, 434 (2018) 37-59.
[73] C.M. Chew, M.K. Aroua, M.A. Hussain, A practical hybrid modelling approach for the prediction of potential fouling parameters in ultrafiltration membrane water treatment plant, J. Ind. Eng. Chem., 45 (2017) 145-155.
[74] H. Amjad, Z. Khan, V.V. Tarabara, Fractal structure and permeability of membrane cake layers: Effect of coagulation–flocculation and settling as pretreatment steps, Sep. Purif. Technol., 143 (2015) 40-51.